

On the fundamentality of the radial acceleration relation for late-type galaxy dynamics

Richard Stiskalek^{1*} and Harry Desmond^{2†}

¹*Astrophysics, University of Oxford, Denys Wilkinson Building, Keble Road, Oxford, OX1 3RH, UK*

²*Institute of Cosmology & Gravitation, University of Portsmouth, Dennis Sciama Building, Portsmouth, PO1 3FX, UK*

Accepted XXX. Received YYY; in original form ZZZ

ABSTRACT

Galaxies have been observed to exhibit a level of simplicity unexpected in the complex galaxy formation scenario posited by standard cosmology. This is particularly apparent in their dynamics, where scaling relations display much regularity and little intrinsic scatter. However, the parameters responsible for this simplicity have not been identified. Using the Spitzer Photometry & Accurate Rotation Curves galaxy catalogue, we argue that the radial acceleration relation (RAR) between galaxies’ baryonic and total dynamical accelerations is the fundamental 1-dimensional correlation governing the radial (in-disk) dynamics of late-type galaxies. In particular, we show that the RAR cannot be tightened by the inclusion of any other available galaxy property, that it is the strongest projection of galaxies’ radial dynamical parameter space, and that all other statistical radial dynamical correlations stem from the RAR plus the non-dynamical correlations present in our sample. We further provide evidence that the RAR’s fundamentality is unique in that the second most significant dynamical relation does not possess any of these features. Our analysis reveals the root cause of the correlations present in galaxies’ radial dynamics: they are nothing but facets of the RAR. These results have important ramifications for galaxy formation theory because they imply that to explain statistically late-type galaxy dynamics within the disk it is necessary and sufficient to explain the RAR and lack of any significant, partially independent correlation. While simple in some modified dynamics models, this poses a challenge to standard cosmology.

Key words: galaxies: kinematics and dynamics – dark matter – methods: data analysis

1 INTRODUCTION

A key task of astrophysics is to test the galaxy formation scenario posited by the concordance Λ Cold Dark Matter model of cosmology (Λ CDM; Rees & Ostriker 1977; White & Rees 1978; White & Frenk 1991). This may be done by studying unusual or otherwise highly constraining individual or small sets of objects, for example satellites in coherent planes (Pawlowski 2018), tidal dwarf galaxies (Bournaud 2010), dark matter deficient galaxies (van Dokkum et al. 2018), massive high-redshift galaxies (Lovell et al. 2023) and large clusters (Asencio et al. 2021). Alternatively one may ask whether the galaxy population as a whole is as expected in Λ CDM. A key feature of galaxy formation in Λ CDM is that it is highly stochastic: not only do the properties of galaxies depend on the complex merger and mass accretion histories of the dark matter haloes in which they live, but chance baryonic phenomena such as supernova and feedback from active galactic nuclei can heat and redistribute mass, significantly altering galaxies’ photometry and kinematics. One way to

test the model is, therefore, to ask whether this complexity is manifest in galaxy phenomenology.

Surprisingly, galaxies are observed to be rather simple systems. This is most readily shown by applying the principal component analysis (PCA; F.R.S. 1901; Hotelling 1936) to galaxy photometry, which calculates the fraction of the covariance in the data that may be accounted for by selected linearly combinations of fluxes in various bands. On multiple data sets and a wide range of variations of the basic technique (e.g. including derived quantities such as star formation rate, size, gas mass and morphology) it is found that only 1–3 principal components are required to explain the great majority ($\gtrsim 90$ per cent) of the data covariance (Disney et al. 2008; Conselice 2006; Garcia-Appadoo et al. 2009; Whitmore 1984; Brosche 1973; Bujarrabal et al. 1981; Chang et al. 2010; Cooray et al. 2022). Nonlinear dimensionality reduction techniques such as variational auto-encoders and self-organizing maps have also been applied, and the results extended to galaxies’ spectra (Portillo et al. 2020; Vanderplas & Connolly 2009; in der Au et al. 2012; Davidzon et al. 2022; Hemmati et al. 2019; Rahmani et al. 2018). These studies again indicate that fewer pieces of information are required to reproduce galaxy properties at high fidelity than would

* richard.stiskalek@physics.ox.ac.uk

† harry.desmond@port.ac.uk

be expected in a model where the entire past history of the galaxy and its halo is important.

These findings have analogues in galaxy kinematics, which may be viewed as the set of correlations between the internal motions of galaxies, tracing the underlying potential, and their baryonic mass distributions. To first order the radial kinematics can be summarized by a characteristic velocity and the mass distribution by a total mass and size, leading to the Tully–Fisher relation (TFR; Tully & Fisher 1977) for late-type galaxies and the fundamental plane (FP; Djorgovski & Davis 1987; Dressler et al. 1987) for early-types. The baryonic TFR has very small intrinsic scatter and is a near-perfect power-law over five decades of mass (McGaugh et al. 2000; McGaugh 2012), with few clear outliers (Mancera Piña et al. 2019, 2020). This essentially indicates that two independent degrees of freedom suffice to explain the data (the normalization and power-law index), and perhaps more significantly that at fixed mass surface brightness is asymptotically irrelevant for the rotation velocity (Lelli et al. 2016b; Desmond et al. 2019). The FP is a planar manifold in {mass, velocity, size} space, also with very small intrinsic scatter and a tilt relative to the expectation from the Newtonian virial theorem (Pizagno et al. 2007; Cappellari et al. 2013; Desmond & Wechsler 2017).

In late-type galaxies, the global radial (i.e. in-disk) kinematic behaviour is subsumed by a local relation between the baryonic (g_{bar}) and dynamical (g_{obs}) centripetal acceleration across rotation curves (RCs) known as the mass discrepancy–acceleration or radial acceleration relation (RAR; Milgrom 1983a; Sanders 1990; McGaugh 2004; Lelli et al. 2017). This is highly regular and possesses little intrinsic scatter, and may be fit near-perfectly by functions with only 1–2 free parameters (Lelli et al. 2017; Desmond et al. 2023). It has recently been shown that the intrinsic or underlying RAR—obtained by marginalizing over all relevant galaxy variables—has a scatter of 0.034 ± 0.002 dex around a 1-parameter function in the Spitzer Photometry & Accurate Rotation Curves (SPARC; Lelli et al. 2016a) sample, making it the tightest known dynamical galaxy scaling relation (Desmond 2023). Evidence is growing that early-type galaxies in fact follow the same RAR as late-types (Lelli et al. 2017; Shelest & Lelli 2020; Chae et al. 2019, 2020a; Tian & Ko 2017).

Without a clear prediction or explanation of galaxies’ simplicity within concordance cosmology it is important to study it empirically in an attempt to learn the features that govern it. These are the features a theory must account for to explain galaxy phenomenology, and may also provide new empirical tools for measuring galaxies’ properties (as the TFR and FP afford redshift-independent distance probes). Motivated by the striking properties of the RAR, we test here the hypothesis that it is the “fundamental” 1-dimensional relation in (late-type) radial galaxy dynamics, meaning that it alone accounts statistically for *all* correlations involving dynamics within the disk. If this is so, then the full set of such correlations amount to nothing more than the RAR in conjunction with the non-dynamical correlations present in the sample, and explaining them is tantamount to explaining the RAR (and lack of any competing correlation). We break this question into two which we tackle in turn:

(i) Do the residuals of the RAR have no statistically significant correlation with any other galaxy or environmental

property? (If they did, the RAR is not fundamental because it can be augmented by inclusion of those properties.)

(ii) Is the RAR the tightest projection of galaxies’ radial dynamical parameter space, and can all other projections be explained by the RAR in conjunction with non-dynamical correlations present among the galaxy properties? (If not, there is at least one other relation as important as the RAR.)

We consider an affirmative answer to both questions to be necessary and sufficient to establish the fundamentality of the RAR. We then further assess whether fundamentality is a *unique* property of the RAR, or whether there are any other (partially) independent relations also satisfying these fundamentality conditions. These aims are achieved by means of non-linear machine learning algorithms.

The structure of the paper is as follows. In Section 2 we describe the SPARC galaxy sample on which we base our analysis. Section 3 lays out our methods, including the statistics and methods we employ and the generation of mock data to validate our procedure. Section 4 contains our results—separately for each question above—while Section 5 discusses the broader ramifications of our results, caveats and systematic uncertainties, and useful further work. Section 6 concludes. The reader without particular interest in the technicalities of the methods is advised to skip Section 3 and refer back to it as and when it is mentioned in Section 4. For brevity, we will henceforth refer to statistically averaged, equilibrium radial motions within the plane of the disk simply as “dynamics”; these caveats are discussed further in Section 5.2.1. All logarithms are base-10.

2 OBSERVATIONAL DATA

We utilize the SPARC database¹ containing 175 galaxy RCs with *Spitzer* 3.6 μm photometry (Lelli et al. 2016a). Following Lelli et al. (2017), we exclude galaxies with a quality flag of 3 (large asymmetry, non-circular motion, large offset between stellar and HI distribution), inclination less than 30 degrees, or fractional uncertainty on the observed rotational velocity exceeding 10 per cent. We are left with 2,696 RC samples from 147 late-type galaxies. We define the total disk and bulge surface brightness as $\Sigma_{\text{tot}} = \Sigma_{\text{disk}} + \Sigma_{\text{bulge}}$. Unresolved disk and bulge surface brightness, Σ_{disk} and Σ_{bulge} , are replaced with a single value below the minimum resolved value of $0.01 L_{\odot}/\text{pc}^2$ (which has no effect on our results).

Table 1 lists the parameters used for predicting galactic dynamical variables and searching for residual correlations. Local parameters (one value per RC point per galaxy) are listed above the line, while galaxy-wide parameters (one value per galaxy) are listed below it. We take the logarithm of properties with a dynamical range spanning several orders of magnitude, as indicated in the final column.

Each of these parameters is contained in the SPARC database except for the gravitational field at the SPARC galaxies’ position, sourced by surrounding baryonic mass. This is calculated in Chae et al. (2021) and will allow us to assess whether g_{obs} depends on the external field. At fixed internal mass distribution this would constitute a violation of the strong equivalence principle, as has been argued for

¹ <http://astroweb.cwru.edu/SPARC/>

Label	Property	Logarithm?
g_{bar}	Baryonic centripetal acceleration	✓
r/R_{eff}	Radial distance normalized to R_{eff}	✓
Σ_{disk}	Disk surface brightness	✓
Σ_{bulge}	Bulge surface brightness	✓
Σ_{tot}	Total surface brightness	✓
D	Galaxy distance	
i	Galaxy inclination	
$L_{3.6}$	Galaxy luminosity at $3.6 \mu\text{m}$	✓
R_{eff}	Galaxy effective radius at $3.6 \mu\text{m}$	✓
M_{HI}	Galaxy neutral hydrogen mass	✓
T	Galaxy type	
e_{N}	External Newtonian field of baryons	✓

Table 1. Summary of features considered as potential predictors of galactic dynamical variables. A logarithmic transformation is applied to the indicated features with a wide dynamical range before inputting them into regression models.

by Chae et al. (2020b, 2021, 2022). We adopt the results assuming maximal clustering of unseen baryons with visible structures, which maximizes data agreement using the fitting function of Chae & Milgrom (2022), as shown in Chae et al. (2021, 2022). The results assuming no clustering of unseen baryons are however very similar. The values of e_{N} are available for only 90 galaxies in the Sloan Digital Sky Survey (SDSS; Kollmeier et al. 2017) footprint; when including e_{N} as a feature, we fill the missing values with the median of the measured sample.

We calculate the uncertainty of g_{bar} and g_{obs} as

$$\delta g_{\text{bar}} = \frac{1}{10} \frac{\Upsilon_{\text{gas}} V_{\text{gas}}^2}{r} + \frac{1}{4} \frac{(\Upsilon_{\text{disk}} V_{\text{disk}}^2 + \Upsilon_{\text{bulge}} V_{\text{bulge}}^2)}{r}, \quad (1a)$$

$$\delta g_{\text{obs}} = g_{\text{obs}} \sqrt{4 \frac{\delta V_{\text{obs}}^2}{V_{\text{obs}}^2} + 4 \frac{\delta i^2}{\tan^2 i} + \frac{\delta D^2}{D^2}}, \quad (1b)$$

where the numerical factors in δg_{bar} correspond to the mass-to-light ratio uncertainties. We assume no further uncertainty on the velocity components; however, the calculation in Lelli et al. (2016a) requires a disk thickness which is expected to introduce unmodelled uncertainty to the baryonic velocities at the $\sim 10 - 15$ per cent level in the innermost region (F. Lelli, priv. comm.). These uncertainties dominate those from other sources such as the covariances across RCs due to HI interferometry and the integral equations used to calculate V_{disk} and V_{bulge} (Lelli et al. 2016a; Lelli 2023). We propagate the uncertainty as $\delta \log g_{\text{bar}} = \delta g_{\text{bar}} / (g_{\text{bar}} \ln 10)$ and similarly for $\delta \log g_{\text{obs}}$.

3 METHODOLOGY

In this section we detail the statistical tools used in our analysis. We discuss the analytic functions used to approximate the RAR, the partial correlation (PC) analysis, machine learning regression techniques, the loss function, and the generation of SPARC-like mock data with controlled dynamics. The main thrust of our analysis, including its results, can be found in Section 4, which refers back to this section for details.

3.1 RAR analytic approximations

We consider two functions known to describe the RAR well. The first is the RAR interpolating function (RAR IF) introduced by Lelli et al. (2017):

$$g_{\text{obs}} = \frac{g_{\text{bar}}}{1 - e^{-\sqrt{g_{\text{bar}}/a_0}}}, \quad (2)$$

where $a_0 \sim 10^{-10} \text{ m/s}^2$ is a global characteristic acceleration scale. The second is the simple interpolating function + external field effect (Simple IF + EFE), which includes an additional parameter e_{N} causing a downturn in the RAR at low g_{bar} (Milgrom 1983c; Chae & Milgrom 2022):

$$g_{\text{obs}} = g_{\text{bar}} \left(\frac{1}{2} + \left(\frac{1}{4} + \left(\left(\frac{g_{\text{bar}}}{a_0} \right)^2 + (1.1e_{\text{N}})^2 \right)^{-\frac{1}{2}} \right)^{\frac{1}{2}} \right) \times \left(1 + \tanh \left(\frac{1.1e_{\text{N}}}{g_{\text{bar}}/a_0} \right)^{1.2} \times \left(-\frac{1}{3} \right) \times \left(\left(\left(\frac{g_{\text{bar}}}{a_0} \right)^2 + (1.1e_{\text{N}})^2 \right)^{-\frac{1}{2}} \right) \left(\frac{1}{4} + \left(\left(\frac{g_{\text{bar}}}{a_0} \right)^2 + (1.1e_{\text{N}})^2 \right)^{-\frac{1}{2}} \right)^{-\frac{1}{2}} \right) \frac{1}{1 + \left(\frac{1}{2} + 2 \left(\left(\frac{g_{\text{bar}}}{a_0} \right)^2 + (1.1e_{\text{N}})^2 \right)^{-\frac{1}{2}} \right)^{\frac{1}{2}}}.$$

e_{N} may be considered as either a global constant or a galaxy-specific parameter, leading to a slightly distinct RAR for each galaxy. Studies of the SPARC data have provided evidence for the effect of e_{N} Chae et al. (2020b, 2021, 2022); Chae & Milgrom (2022).

These empirical fitting functions hold particular significance in the theory of Modified Newtonian Dynamics (MOND; Milgrom 1983a,c,b), an alternative to the Newtonian gravity on which General Relativity and hence ΛCDM is based. Eq. (2) is a simple instantiation of the fundamental MOND postulate that $g_{\text{obs}} = g_{\text{bar}}$ for $g_{\text{bar}} \gg a_0$ and $g_{\text{obs}} = \sqrt{g_{\text{bar}} a_0}$ for $g_{\text{bar}} \ll a_0$. Eq. (3) models the external field effect (EFE) in the Aquadratic Lagrangian (AQUAL; Bekenstein & Milgrom 1984) theory: due to the nonlinear acceleration-based modification, galaxies with identical mass distributions but differing environments will have different internal dynamics. A stronger external field pushes a galaxy closer to the Newtonian limit and hence produces a fall-off in the RAR at low g_{bar} . In this interpretation, $e_{\text{N}} \equiv g_{\text{ext}}/a_0$, where g_{ext} represents the strength of the Newtonian gravitational field sourced by the surrounding baryonic mass.

3.2 Partial correlation

We employ a one-sided PC analysis (Baba et al. 2004) to investigate the correlation between g_{obs} and other galaxy properties $\{x_k\}$ at fixed g_{bar} . We consider the RAR in logarithmic space and define the residuals $\Delta \log g_{\text{obs}} \equiv \log g_{\text{obs}} - \mathcal{F}(\log g_{\text{bar}})$, where \mathcal{F} is a RAR-like function that predicts $\log g_{\text{obs}}$ based on $\log g_{\text{bar}}$. We then compute the g_{bar} -controlled PC between g_{obs} and x_k as the Kendall rank correlation $\tau \in [-1, 1]$ of $\Delta \log g_{\text{obs}}$ and x_k , which we denote $\tau(g_{\text{obs}}, x_k | g_{\text{bar}})$ (Kendall 1938). This choice of correlation coefficient is motivated by the lack of prior expectation for linear residual correlations and by the greater robustness of the Kendall than Spearman coefficient (Colwell & Gillett 1982;

Puth et al. 2015). The Spearman coefficient yields very similar results.

The PC coefficient does not account for uncertainties, so a non-zero $\tau(g_{\text{obs}}, x_k | g_{\text{bar}})$ does not necessarily indicate a significant relationship between $\Delta \log g_{\text{obs}}$ and x_k . While the correlation coefficient is sensitive to the mean trend, the predictive relationship between specific data realizations might be dominated by noise and the standard p -values therefore unreliable. Instead, we assess the impact of uncertainties on the PC by generating mock data using the Simple IF + EFE with the SPARC error model (Section 3.5) and calculate the corresponding PC coefficients to compare to those of the real data. This yields the distribution of PC coefficients corresponding to a SPARC-like data set that explicitly contains no dynamical correlations besides the RAR. If the data PC coefficient is a typical draw from the mock distribution, SPARC is a typical realization of a galaxy population in which dynamics is set entirely by the RAR.

3.3 Design of machine learning regressors

We investigate the relationship between baryonic and dynamical properties using a fully connected, feed-forward neural network (NN) and decision tree-based regression techniques. The baryonic features considered as potential predictors of a target dynamical quantity are presented in Table 1. For galaxy-wide properties, each RC sample is assigned its galaxy's value. All properties are scaled to be zero-centred with a variance of unity.

3.3.1 Neural network architecture

A NN represents a continuous, differentiable mapping: $f : \mathbb{R}^m \rightarrow \mathbb{R}^n$ with m input and n output nodes. The simplest fully connected, feed-forward NN without hidden layers relates an m -dimensional input feature vector to an n -dimensional prediction by passing the sum of the product of the feature vector with a weight matrix and a constant bias factor through a non-linear activation function (e.g., sigmoid, hyperbolic tangent; Bishop & Nasrabadi 2007; Roberts et al. 2021). The weights and biases are trainable parameters optimized by minimizing a loss function on training samples through back-propagation (Rumelhart et al. 1986; see Section 3.4). In NNs with hidden layers, the output of a previous layer serves as input for the subsequent layer.

Our chosen NN architecture is as follows. The network's input layer is normalizing: it adjusts the samples' mean to zero and variance to unity. The network comprises two parallel components with outputs that are combined: a fully-connected NN with a wide hidden layer, and a single-node hidden layer with no activation, functioning as a linear operation. For the wide hidden layer, we employ the leaky rectified linear unit (LReLU) activation function.

$$\phi(x) = \begin{cases} x & \text{if } x \geq 0 \\ \alpha x & \text{if } x < 0, \end{cases} \quad (4)$$

where we choose $\alpha = -0.2$. In contrast to the conventional ReLU ($\alpha = 0$), the LReLU has a non-vanishing gradient if $x < 0$. We add a dropout layer following the wide hidden layer, which randomly sets a fraction f of nodes' inputs to 0 and scales the remaining inputs by $1/(1-f)$ (Gal

& Ghahramani 2015). Additionally, we apply an l^2 norm to regularize the weights with $\lambda = 0.01$. The loss function in Eq. (9), which depends on the derivative of the NN prediction with respect to its input, is optimized using the Adam stochastic optimizer (Kingma & Ba 2014) with default hyperparameters² and a cosine decay learning schedule (Loshchilov & Hutter 2016). We implement the NN architecture in TensorFlow³ (Abadi et al. 2015) and optimize the width of the hidden layer and the dropout rate (Section 3.3.3).

Training is performed over the training samples containing 60 per cent of galaxies. This fraction is chosen by fitting the RAR as a function of it and optimizing the resulting goodness-of-fit to maximize the models' generalization to unseen observations. We verify robustness of our conclusions to this choice. The train-test split is performed at the galaxy level, rather than on separate RC samples, to prevent information leakage between the sets otherwise introduced by the galaxy-wide properties. We choose a batch fractional size of 1/3, with one epoch consisting of a single pass through all three batches. The training process continues until the validation loss has not decreased for at least 2,000 epochs, after which the optimal set of weights is restored. Due to the limited sample size, the validation loss is evaluated on the entire training data set.

3.3.2 Decision tree models

Decision tree regressors are grown by recursively partitioning samples into increasingly homogeneous subsamples minimizing a specific loss function, such as the weighted variance of the descendant nodes' samples. Predictions are acquired by traversing a path within the tree and procuring the mean value of a terminal leaf. The random forest (RF; Breiman 2001) is a widely employed model. In it, an ensemble of decision trees is constructed, with each tree trained on bootstrap aggregated resamples of the training data and a randomly selected number of features for optimal split determination at each node. This approach mitigates the over-fitting issue commonly encountered in individual decision trees. Another ensemble model is the extra-trees (ET; Geurts et al. 2006). This neither performs bootstrap resampling nor seeks an optimal split, but instead randomly selects a subset of features at each node, assigns them a random split, and divides the samples based on the feature whose split minimizes the loss function. An alternative to constructing large ensembles of independent decision trees is to consider sequential, gradient-boosted trees where each tree is designed to predict the residuals of its predecessors (Friedman 2001, 2002).

At first glance, tree-based regressors possess an appealing property: the ability to provide feature importance scores. The feature importance is the average summed impurity decrease (homogeneity increase) across all nodes split along a particular feature, averaged over all trees in the ensemble. An alternative metric not limited to tree-based regressors, permutation importance, is computed by permuting a feature, thereby randomizing its correlation with both the re-

² https://www.tensorflow.org/api_docs/python/tf/keras/optimizers/Adam

³ <https://www.tensorflow.org>

maining features and the target, and subsequently observing the model's relative predictive loss. Notably, the model is not retrained during this process, and the procedure is repeated multiple times to obtain a reliable estimate. High permutation importance indicates that the model's predictive power diminishes upon feature permutation, while low permutation importance suggests that the feature is either irrelevant or strongly correlated with another feature. However, interpreting the allocation of either feature or permutation importance to individual features can be challenging when features exhibit strong mutual correlations. Explainable machine learning methods, such as Shapley additive explanation (SHAP; Lundberg & Lee 2017; Lundberg et al. 2020) attempt to address this issue, although their interpretation is not always straightforward (Krishna et al. 2022). Because of this, we do not put strong emphasis on the explainability aspect of our methods and will only briefly rely on the permutation importance score in Section 4.2.

We employ the ET model `ExtraTreesRegressor` from `scikit-learn`⁴ (Pedregosa et al. 2011), and the extreme gradient boosting decision tree model `XGBRegressor` from the `XGBoost`⁵ library (Chen & Guestrin 2016, denoted XGB hereafter). We do not use the RF as we find its behaviour near-identical to the ET. We again allocate 60 per cent of galaxies to the training set and the remainder to the test set.

3.3.3 Hyperparameter selection

The efficacy and accuracy of any machine learning (ML) regressor hinges upon the appropriate selection of its hyperparameters, describing the architecture of the algorithm. Striking an optimal balance in the complexity is crucial, as overly simplistic models may fail to capture relevant features of the data while excessively complex ones risk overfitting and hence poor extrapolation or generalization. We employ `Optuna`⁶ for hyperparameter optimization, which facilitates efficient exploration of high-dimensional hyperparameter spaces (Akiba et al. 2019). The optimal set of hyperparameters is determined via cross-validation, in each case optimizing a loss function described in Section 3.4. Because the training of a NN is more computationally demanding than that of ET and XGB, we automatically optimize only the hidden layer width and dropout rate.

We conduct 25 trials using `Optuna`, with each trial involving 50 re-trainings of the NN on the same data to account for stochasticity. For the ET and XGB we execute 10,000 trials without any retraining in each trial. The hyperparameters that we optimize for each model are presented in Table 2, which also includes the best parameters for the prediction of g_{obs} from g_{bar} (i.e. the RAR).

3.4 Scoring regressors

Fitting a model $f : \mathbb{R} \rightarrow \mathbb{R}$, be it an analytic function or machine learning regressor, requires a loss function to minimize. In machine learning this is typically considered to be

the mean square error (or equivalently coefficient of determination R^2) between the data and prediction. This however ignores the measurement uncertainties which are crucial for reliable inference. We therefore consider a Gaussian likelihood function allowing for uncertainties in both the independent (x) and dependent (y) variable. This necessitates introducing latent variables for the true location of the independent variable, x_t , on which the full likelihood function depends (e.g. Berger et al. 1999). To eliminate these nuisance parameters one can either marginalize over them with a suitable prior or fix them to their maximum likelihood values as a function of the inferred parameters to make a profile likelihood. The profile likelihood is unbiased in parameters describing the shape of the function because its maximum is by construction at the same point in parameter space as the original likelihood's, and the underestimation of uncertainties is unimportant when one considers, as we do, only best-fit values.

The likelihood of observed values x, y given x_t and the functional fit f is

$$p(x, y | x_t, I) \propto \exp \left(-\frac{(y - f(x_t))^2}{2\sigma_y^2} - \frac{(x - x_t)^2}{2\sigma_x^2} \right), \quad (5)$$

assuming uncorrelated Gaussian distributions for x and y with uncertainties σ_x and σ_y , respectively, and omitting normalization terms. Here, I represents the free parameters of $f(x)$. The maximum likelihood estimate of the true independent variable is given by

$$\hat{x}_t = \arg \max_{x_t} p(x, y | x_t, I). \quad (6)$$

We expand the function $f(x)$ to first order around the observed value x as

$$f(x_t) = f(x) + (x_t - x) \left. \frac{df}{dx} \right|_x + \dots \quad (7)$$

As the RAR is approximately composed of two linear segments in log-space (and other dynamical correlations are similarly near power-laws), the error induced by the neglected higher order terms is negligible. Substituting the above two equations into the joint probability, we obtain the profile likelihood:

$$p_{\text{prof}}(x, y | I) \propto \exp \left(-\frac{1}{2} \frac{(y - f(x))^2}{\sigma_y^2 + \sigma_x^2 \left. \frac{df}{dx} \right|_x^2} \right), \quad (8)$$

where $\left. \frac{df}{dx} \right|_{x_0}^2$ projects the uncertainty of x along y . For a set of statistically independent observations $\{x, y, \sigma_x, \sigma_y\}$, the overall likelihood is given by their product. A derivation of the alternative likelihood with x_t integrated out using a uniform prior, which performs better in the presence of intrinsic scatter, can be found in Desmond et al. (2023).

In accordance with ML terminology, we introduce a loss function \mathcal{L} as the negative profile log-likelihood

$$\mathcal{L}(x, y | I) \equiv \frac{1}{2} \frac{(y - f(x))^2}{\sigma_y^2 + \sigma_x^2 \left. \frac{df}{dx} \right|_x^2}, \quad (9)$$

which we denote henceforth simply as \mathcal{L} . This is equivalent to the common least-squares (or χ^2) loss with a sample weight of $1/\sigma^2$ where

$$\sigma^2 \equiv \sigma_y^2 + \sigma_x^2 \left. \frac{df(x)}{dx} \right|_x^2. \quad (10)$$

⁴ <https://scikit-learn.org/>

⁵ <https://xgboost.readthedocs.io/>

⁶ <https://optuna.org>

	Hyperparameter	Options	Best for RAR
TensorFlow NN	width	$\mathbb{N}(8, 128)$	16
	dropout_rate	$\mathbb{R}(0.001, 0.10)$	0.05
ExtraTreesRegressor	n_estimators	$\mathbb{N}(64, 128)$	92
	max_depth	$\mathbb{N}(2, 16)$	8
	min_samples_split	$\mathbb{N}(2, 32)$	2
	max_features	{sqrt, log2, None}	sqrt
	min_impurity_decrease	$\mathbb{R}(10^{-14}, 0.5)$	4.2×10^{-5}
	ccp_alpha	$\mathbb{R}(10^{-14}, 0.5)$	4.4×10^{-12}
	max_samples	$\mathbb{R}(0.1, 0.99)$	0.94
XGBoostRegressor	n_estimators	$\mathbb{N}(16, 128)$	125
	max_depth	$\mathbb{N}(2, 8)$	4
	booster	{gbtree, dart}	dart
	learning_rate	$\mathbb{R}(0.01, 0.99)$	0.94
	gamma	$\mathbb{R}(0, 10)$	1.6
	min_child_weight	$\mathbb{R}(0.5, 2.5)$	2.14
	subsample	$\mathbb{R}(0.5, 1)$	0.56

Table 2. Hyperparameter ranges of the NN, ET and XGB regressors that are optimized with **Optuna** (Section 3.3), with \mathbb{N} and \mathbb{R} representing integer and real ranges, respectively. The rightmost column shows the best hyperparameters for predicting g_{obs} from g_{bar} , i.e. the RAR relation.

To propagate the uncertainty of the independent variable, it is essential that the regressor $f(x)$ be differentiable. This condition is satisfied for our analytic functions as well as our NN thanks to automatic differentiation (e.g. [Gunes Baydin et al. 2015](#)). Our ET and XGB models are however non-differentiable and so we cannot directly minimize Eq. (9). We therefore approximate the gradient with an analytic expression prior to model fitting and set the inverse of Eq. (10) to be the sample weight. For the RAR, we use the gradient of the RAR IF, assuming a best-fit value of $a_0 = 1.118 \times 10^{-10} \text{ m/s}^2$ obtained by fitting this function to the full SPARC data set using Eq. (9). For multi-dimensional cases where $f: \mathbb{R}^m \rightarrow \mathbb{R}$ with $m > 1$, the loss function in Eq. (9) is extended by summing over the square of the product of gradient and uncertainty in each independent variable. In certain instances we will ignore the uncertainty in the independent variable (i.e. $\sigma_x = 0$), denoting this loss as

$$\mathcal{L}_0 = \frac{1}{2} \frac{(y - f(x))^2}{\sigma_y^2}. \quad (11)$$

We verify that these choices have little effect on the minimum loss or the parameter values at which it occurs.

3.5 Mock data

To quantify sample variance and aid in interpreting our results, we generate mock data that by construction exhibit a specific dynamical correlation only. These differ only in the values of V_{obs} and their correlations with other variables, and are otherwise generated according to the SPARC error model. The first set of mocks calculates V_{obs} through the $g_{\text{bar}} - g_{\text{obs}}$ correlation of the data (i.e. the RAR) and the second through the $\Sigma_{\text{tot}} - J_{\text{obs}}$ relation, where J_{obs} is the jerk V_{obs}^3/r^2 . The reason for the latter choice is that $\Sigma_{\text{tot}} - J_{\text{obs}}$ will be found in Section 4.2 to be the second strongest dynamical correlation in SPARC; we wish to see whether either of these relations is sufficient to account for the other correlations. We do not model intrinsic scatter in either relation, which (at the

level at which it is present in SPARC) would simply weaken slightly the strengths of the correlations.

Both mock data sets account for the covariance of V_{bar} and V_{obs} across a single galaxy’s RC induced by uncertainties in distance (D), inclination (i), mass-to-light ratios (gas Υ_{gas} , disk Υ_{disk} , bulge Υ_{bulge}), and luminosity ($L_{3.6}$) by directly sampling them for each galaxy from their prior distributions. We assume Gaussian distributions for all galaxies and denote with an overbar the prior mean as taken from SPARC:

$$D \leftarrow \mathcal{G}(\bar{D}, \delta D), \quad (12a)$$

$$i \leftarrow \mathcal{G}(\bar{i}, \delta i), \quad (12b)$$

$$\log \Upsilon_{\text{gas}} \leftarrow \mathcal{G}(\log 1.0, 0.04), \quad (12c)$$

$$\log \Upsilon_{\text{disk}} \leftarrow \mathcal{G}(\log 0.5, 0.10), \quad (12d)$$

$$\log \Upsilon_{\text{bulge}} \leftarrow \mathcal{G}(\log 0.7, 0.10), \quad (12e)$$

$$L_{3.6} \leftarrow \mathcal{G}(\bar{L}_{3.6}, \delta L_{3.6}), \quad (12f)$$

where the standard deviation of $\log \Upsilon_{\text{gas}}$ corresponds to a 10 per cent uncertainty on Υ_{gas} .

We calculate the mock baryonic acceleration and surface brightness as

$$g_{\text{bar}} = \frac{L_{3.6}}{\bar{L}_{3.6}} \left(\sum_{\text{X}} \frac{\Upsilon_{\text{X}} V_{\text{X}} |V_{\text{X}}|}{\bar{r}} \right) + \frac{\Upsilon_{\text{gas}} V_{\text{gas}} |V_{\text{gas}}|}{\bar{r}}, \quad (13a)$$

$$\Sigma_{\text{tot}} = \left(\frac{L_{3.6}}{\bar{L}_{3.6}} \right) \bar{\Sigma}_{\text{tot}}. \quad (13b)$$

where $\text{X} \in \{\text{disk}, \text{bulge}\}$. We scale the disk and bulge contributions along with the surface brightness by the observational error on luminosity, which is however very small. g_{bar} and Σ_{tot} are distance independent; in case of the former velocities are proportional to \sqrt{D} and galactocentric separation is proportional to D . We generate 100 mock realizations of the SPARC data set and calculate the mean and standard deviation among them.

3.5.1 Imposing the RAR

For this mock data set we employ a fitting function \mathcal{F} , specifically the RAR IF of Eq. (2) or Simple IF + EFE of Eq. (3), to connect the sampled baryonic acceleration to the “true” total acceleration $\langle g_{\text{obs}} \rangle = \mathcal{F}(g_{\text{bar}})$. Considering that $V_{\text{obs}} \propto 1/\sin i$ and $r \propto D$, we adjust the mock total acceleration for the sampled inclination and distance:

$$g_{\text{obs}} \leftarrow \mathcal{G} \left(\langle g_{\text{obs}} \rangle \left(\frac{\sin i}{\sin \bar{i}} \right)^2 \left(\frac{D}{\bar{D}} \right), \frac{2\delta V_{\text{obs}}}{V_{\text{obs}}} \right), \quad (14)$$

where the standard deviation accounts for the propagated statistical uncertainty of V_{obs} to g_{obs} . The sampled galactocentric distance is $r = r_t D/\bar{D}$. This yields a set of mock “observed” values $\{r, g_{\text{bar}}, g_{\text{obs}}\}$ for the galaxy’s RC generated with \mathcal{F} . When using the Simple IF + EFE to generate the mock data, we have that $g_{\text{obs}} = \mathcal{F}(g_{\text{bar}}, e_N)$, where e_N is sampled according to $\log e_N \leftarrow \mathcal{G}(\log \bar{e}_N, \delta \log e_N)$ given the results of Chae et al. (2021). We set the free parameter a_0 in the mock data by minimizing the loss function Eq. (9) over the entire SPARC data set. For the RAR IF, we obtain $a_0 = 1.118 \times 10^{-10} \text{ ms}^{-2}$, while for the Simple IF + EFE we find $a_0 = 1.170 \times 10^{-10} \text{ ms}^{-2}$. In the latter case we simultaneously fit a global parameter e_N (for which we find $\log e_N = -2.088$), although this is not used in the construction of the mock data. The precise values of these parameters make no difference to the results.

3.5.2 Imposing the $\Sigma_{\text{tot}} - J_{\text{obs}}$ relation

To model the $\log \Sigma_{\text{tot}} - \log J_{\text{obs}}$ relation we fit the relation in SPARC, shown in Fig. 1, with a cubic polynomial by minimizing Eq. (9). This fits the data well and yields coefficients for the cubic, quadratic, linear and constant terms of 4.07, 0.27, 0.08, 0.02. Our results are not significantly affected by the form of the $\Sigma_{\text{tot}} - J_{\text{obs}}$ function provided it captures the mean trend of the data. We use this to calculate the true mock jerk $\langle J_{\text{obs}} \rangle$ from Σ_{tot} . We then determine the “observed” jerk given the inclination and distance for this mock data set, and the statistical uncertainty of V_{obs} , according to:

$$J_{\text{obs}} \leftarrow \mathcal{G} \left(\langle J_{\text{obs}} \rangle \left(\frac{\sin i}{\sin \bar{i}} \right)^3 \left(\frac{D}{\bar{D}} \right)^2, \frac{3\delta V_{\text{obs}}}{V_{\text{obs}}} \right). \quad (15)$$

4 RESULTS

4.1 Residual correlations of the RAR

Our first objective is to investigate the residual correlations in the RAR to determine whether g_{obs} exhibits correlations with any other variables at fixed g_{bar} . The existence of such correlations would disqualify the RAR as fundamental because it would imply that a tighter manifold could be constructed in a higher-dimensional space by incorporating secondary variables. This is analogous to the correlation of velocity dispersion with galaxy size at fixed luminosity in early-type galaxies, which refines the Faber–Jackson relation to the FP (Djorgovski & Davis 1987; Dressler et al. 1987; Bender et al. 1992; Cappellari et al. 2013). To address this, we employ two methods:

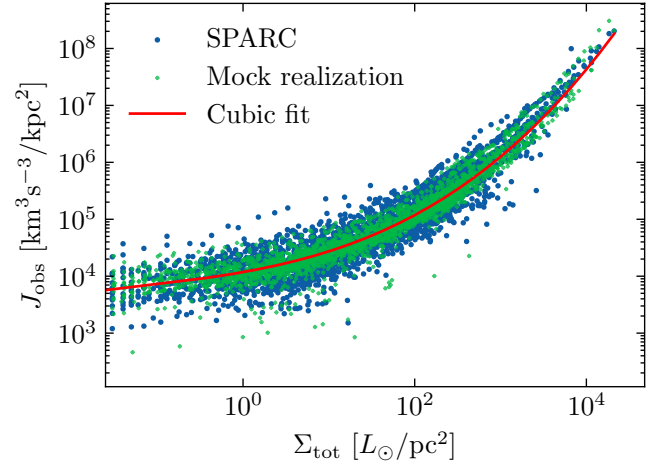


Figure 1. Relation between surface brightness Σ_{tot} and jerk $J_{\text{obs}} = V_{\text{obs}}^3/r^2$ for both SPARC and an example mock realization. The mock data is generated by assuming a cubic $\Sigma_{\text{tot}} - J_{\text{obs}}$ relation (red line) in conjunction with the SPARC error model, as described in the text. This is used as a foil for the RAR mock data to establish which dynamical correlations are primary and which derivable from them.

- (i) compute partial correlation coefficients between g_{obs} and all other accessible variables at fixed g_{bar} , and
- (ii) employ flexible, non-linear machine learning algorithms to determine if the prediction of g_{obs} can be improved by considering additional variables besides g_{bar} .

4.1.1 Partial correlation

We calculate the Kendall correlation coefficient of galaxy properties with the RAR residuals around the RAR IF (Section 3.1): for the details see Section 3.2. In Fig. 2 we present the SPARC PC coefficients as red crosses, and compare them to the expectation from mock data using g_{obs} generated from the Simple IF + EFE (Section 3.5), depicted as blue violins. Although several data PC coefficients are non-zero, this is consistent with the null hypothesis that the real data is drawn from the mocks. The width of the mock PC coefficient distribution is determined by the sensitivity of the respective features to the RAR residuals. All violins in Fig. 2 use the same set of resampled residuals. Thus, given the size of the data set and the uncertainties, the PC analysis reveals no significant secondary correlations in the RAR. We have also tested replacing the RAR IF fit with our machine learning regressors, finding very similar PC values.

We also show mock PC coefficients around the RAR generated from the $\Sigma_{\text{tot}} - J_{\text{obs}}$ relation as vertical bars extending to $\pm 2\sigma$ with dots at the median. We find significantly non-zero mock PC coefficients in case of T , R_{eff} , r/R_{eff} and Σ_{bul} , indicating that a different relation between baryonic and dynamical properties would lead to strong residual correlations in the RAR. We further calculate the PC coefficients of the $\Sigma_{\text{tot}} - J_{\text{obs}}$ relation of the SPARC data by correlating its residuals around the cubic fit of Section 3.5.2 with baryonic properties (not shown). Comparing these with the expectations from the $\Sigma_{\text{tot}} - J_{\text{obs}}$ mocks, we observe the SPARC PC coefficients of T , g_{bar} , Σ_{bul} to be significant at $\geq 3\sigma$. These coefficients in the data are $\tau(J_{\text{obs}}, T|\Sigma_{\text{tot}}) = -0.277$,

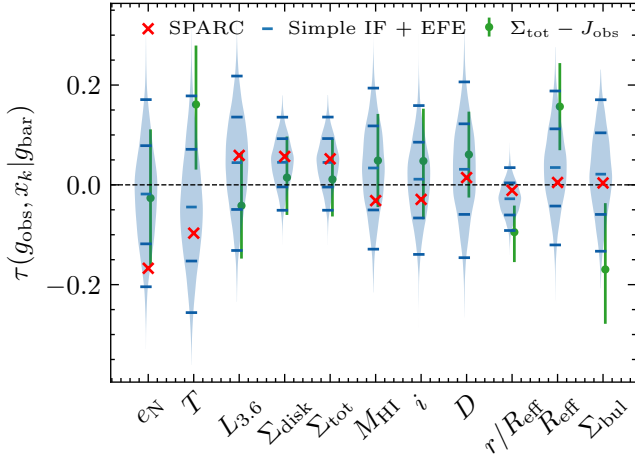


Figure 2. Partial correlation coefficients of the residuals of g_{obs} at fixed g_{bar} (as described by the RAR IF) with various galaxy and environmental features. The SPARC results are shown by red crosses while those of many mock data sets generated by the Simple IF + EFE are shown by blue violins, with the blue ticks indicating the median and 1 and 2σ levels. Vertical green bars show $\pm 2\sigma$ results for mock data with dynamics sourced by the $\Sigma_{\text{tot}} - J_{\text{obs}}$ relation, with dots at the median. No significant deviations of the data from the Simple IF + EFE mocks are observed, indicating that SPARC is a typical realization of a population with dynamics specified fully by the RAR. The only near-significant secondary correlation of g_{obs} is with e_N , hinting at the presence of the EFE. The $\Sigma_{\text{tot}} - J_{\text{obs}}$ mock exhibits non-zero PC coefficients incompatible with the data.

$\tau(J_{\text{obs}}, g_{\text{bar}} | \Sigma_{\text{tot}}) = 0.256$ and $\tau(J_{\text{obs}}, \Sigma_{\text{bul}} | \Sigma_{\text{tot}}) = 0.223$. This shows that the RAR is special in not having any residual correlations: it is not simply that such correlations are washed out by measurement uncertainties or the mixing of different galaxy types in SPARC.

For the RAR, the most significant partial correlation in SPARC, at roughly the 2σ level given the RAR mock data, is $\tau(g_{\text{obs}}, e_N | g_{\text{bar}}) \approx -0.2$, suggesting an anti-correlation between g_{obs} at fixed g_{bar} and e_N . This is as expected from the EFE. Surprisingly, however, the mock PC of e_N is approximately centred at 0 even though it is generated using the Simple IF + EFE function with the best-fit (max clustering) values of e_N from [Chae et al. \(2021\)](#). One would expect a negative PC coefficient $\tau(g_{\text{obs}}, e_N | g_{\text{bar}})$ when the mock data includes a non-zero EFE and the residuals are calculated using the RAR IF fit, as increasing e_N lowers g_{obs} at low g_{bar} . However, we show in Fig. 3 that this effect is washed away by the systematic uncertainties in distance and inclination, as well as the statistical uncertainty in V_{obs} . We show this by sequentially increasing each uncertainty from 0 to its SPARC value, while keeping the other uncertainties fixed at 0. Thus, one would not expect to see $\tau(g_{\text{obs}}, e_N | g_{\text{bar}})$ inconsistent with 0 in the real data even if the EFE were present at the level suggested by [Chae et al. \(2021\)](#).

4.1.2 Regression with g_{bar}

We begin our regression analysis by training our machine learning regressors to predict g_{obs} based solely on g_{bar} (see Sections 3.3 and 3.4). This will afford a comparison point

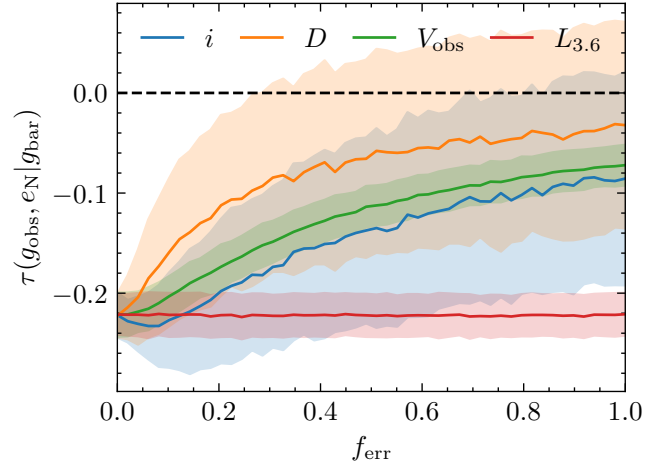


Figure 3. Effect of i , D , V_{obs} , and $L_{3.6}$ uncertainties on the g_{obs} and e_N PC, $\tau(g_{\text{obs}}, e_N | g_{\text{bar}})$. For each parameter, we scale its uncertainty by f_{err} while setting the uncertainty in the remaining parameters to 0. $f_{\text{err}} = 1$ represents the fiducial SPARC uncertainty. While in the noiseless case we would expect to see $\tau < -0.2$ due to the presence of the EFE in these mocks, the uncertainties in i , D , V_{obs} effectively wash it away. The bands show 1σ Monte Carlo uncertainty from 1,000 mock data realizations while the solid lines show the mean.

when incorporating additional features. We generate 10,000 test-train splits and follow the procedure outlined in Section 3.3.3 to determine the optimal hyperparameters for each feature and target.

In Fig. 4, we present the RAR fits using the RAR IF, Simple IF + EFE, NN, ET, and XGB. Note that when fitting the Simple IF + EFE we use a global value of $\log e_N = -2.088$, whereas for the mock data generation using the Simple IF + EFE we use the galaxy-by-galaxy best-fit values of [Chae et al. \(2021\)](#). Due to the EFE, the RAR IF predicts higher values of g_{obs} at low g_{bar} than the Simple IF + EFE, whereas elsewhere it is the Simple IF + EFE that marginally exceeds the RAR IF. The regressors successfully recover the mean trend of the RAR and are approximately consistent with the analytic functions. The NN provides a smooth approximation of the RAR, closely aligned with the Simple IF + EFE. The ET and XGB methods struggle to produce a smooth fit due to their discontinuous nature. They also systematically under-predict g_{obs} at the highest g_{bar} limit and over-predict it at the lowest g_{bar} as a result of interpolating between previously seen samples, driving the edge samples closer to the mean.

In Fig. 5 we show the loss \mathcal{L} from Eq. (9) evaluated on the unseen test samples. Due to the train-test splitting being performed over galaxies rather than the RC samples directly, \mathcal{L} is assessed over a varying number of observations. We instead display the mean test set loss per observation. In the absence of train-test splitting (i.e. simply fitting to the entire data set), the Simple IF + EFE is favoured over the RAR IF, as indicated by the vertical lines in Fig. 5. This is practically guaranteed since the Simple IF + EFE contains an additional free parameter e_N , and reduces to the Simple interpolating function, which closely resembles the RAR IF, when $e_N = 0$. However, the train-test splitting diminishes this preference, resulting in near-identical distributions of \mathcal{L} for the Simple IF

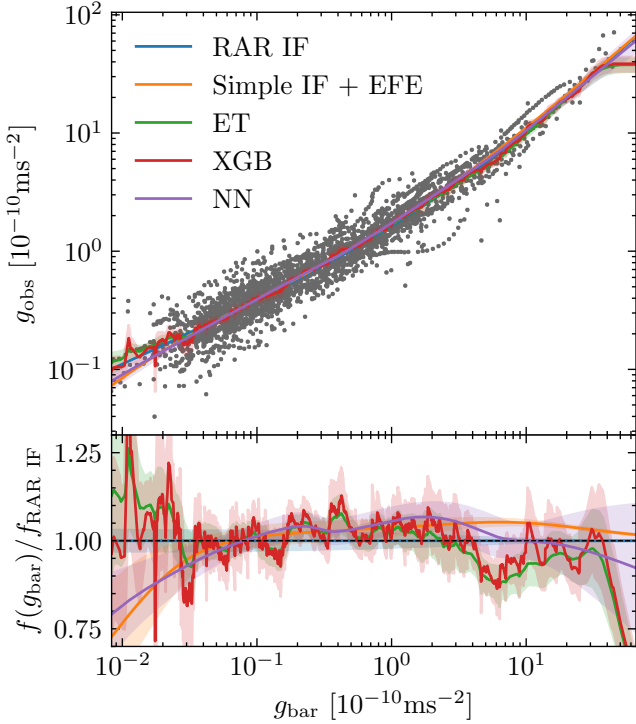


Figure 4. *Upper:* The SPARC RAR (grey points) with various fits overlaid. The lines show predicted values from analytic functions or ML regressors trained on g_{bar} only, averaged over train-test splits. *Lower:* Ratios of predicted g_{obs} with respect to the RAR IF. The bands indicate 1σ variation between the different test-train splits.

+ EFE and RAR IF, with the latter being weakly preferred on average. This suggests that the Simple IF + EFE may be slightly over-fitted.

In examining the goodness-of-fit of the ML models presented in Fig. 5, we find that the NN performs comparably to the Simple IF + EFE. The distributions of \mathcal{L} for the ET and XGB models are systematically higher (i.e. worse) than those of the analytic functions and the NN. We therefore find that none of the ML models can produce a better description of the data than the RAR IF; we discuss this point further in Section 5.2.

4.1.3 Regression with other features

We now extend our analysis by incorporating additional features alongside g_{bar} to predict g_{obs} . The dashed lines in Fig. 5 represent the goodness-of-fit for the ET, XGB, and NN regressors using all available features. Although the peak \mathcal{L} remains relatively unchanged, a more pronounced high-loss tail is observed. Notably, the NN regressor exhibits a significantly degraded performance, with a mean loss several times larger, likely due to convergence issues; hence, it is not displayed in Fig. 5. We also explore dimensionality reduction via PCA for predicting g_{bar} from all features, allowing `Optuna` to optimize the number of dimensions. However, this approach yields no improvement.

The regressors may be confused when presented with all features, especially if several of them are uninformative. We therefore investigate separately the predictivity of g_{obs} using all individual and pairs of features. In Fig. 6, the diagonal

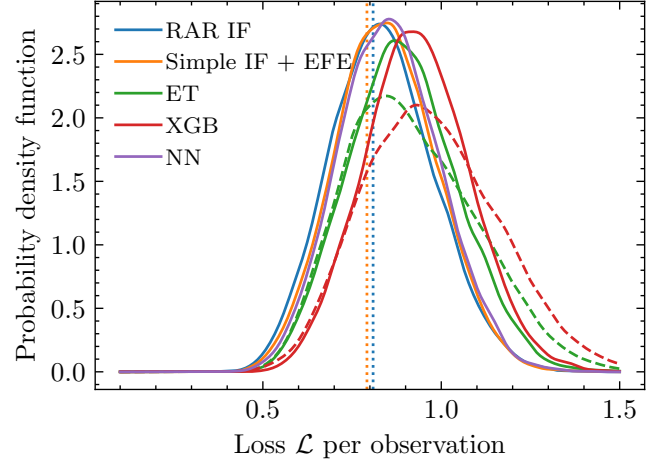


Figure 5. Comparison of RAR average test set loss per data point for 10,000 train-test splits, predicting g_{obs} from g_{bar} only (solid lines) and all features (dashed lines). The vertical lines show the RAR IF and Simple IF + EFE results without train-test splitting. The NN performs comparably to the analytic functions, while ET and XGB perform worse. No ML regressor improves when given features beyond g_{bar} .

cells display the mean loss \mathcal{L}_0 per observation for the ET regressor when predicting g_{obs} using single features. (We verify that other regressors yield similar results.) For simplicity, we present the loss \mathcal{L}_0 without propagating the uncertainty in the independent variable, as an approximate value is sufficient to establish the relative merits of the features. We find that g_{bar} is by far the best individual predictor of g_{obs} . Surface brightness emerges as the next-best predictor, although with a loss nearly an order of magnitude larger. The predictivity of surface brightness can be attributed to its strong correlation with g_{bar} , which is calculated from it. We then assess the predictability of g_{obs} from pairs of features, shown by the off-diagonal elements of Fig. 6. The inclusion of any secondary feature does not enhance the performance of the g_{bar} predictions, but in fact typically degrades it. All pairs of features that do not include g_{bar} exhibit poor goodness-of-fit, and it is rarely the case that a pair of features provides more information on g_{obs} than either one alone. Altogether, similar to the PC analysis, these results indicate that no additional information on g_{obs} can be gleaned from features besides g_{bar} .

4.2 Projections of the dynamical parameter space

We have established the RAR as the fundamental correlation when g_{obs} is the target variable, with g_{bar} fully accounting for g_{obs} up to apparently random noise. Nevertheless, it remains to be determined whether g_{obs} is the optimal target variable. There may exist other dynamical variables more strongly correlated with, or predictable from, baryonic properties, which could potentially imply the RAR as an approximation. To explore this possibility, we generalize our analysis from Section 4.1 to predict an arbitrary dynamical variable, $\mathcal{D}(\alpha, \beta)$, defined as

$$\mathcal{D}(\alpha, \beta) \equiv \frac{V_{\text{obs}}^\alpha}{r^\beta}. \quad (16)$$

This encompasses as special cases V_{obs} ($\alpha = 1, \beta = 0$), g_{obs}

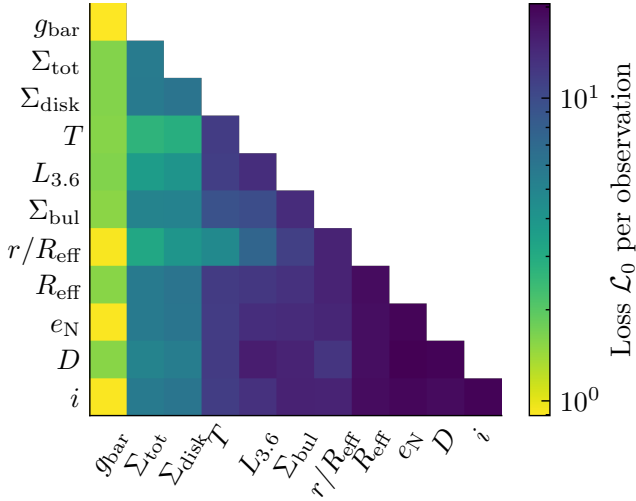


Figure 6. Mean test set loss over 10,000 test-train splits when predicting g_{obs} using the ET regressor with a single feature (diagonal cells) or pairs of features (off-diagonal cells). The diagonal cells are ordered by increasing loss. g_{bar} alone is the optimal predictor: its performance is diminished by combining it with any other feature. No other feature, or combination thereof, yields accurate prediction of g_{obs} . The mean and standard deviation of the four lowest loss (yellow) cells are $g_{\text{bar}} : 0.894 \pm 0.152$; $g_{\text{bar}} + i : 0.910 \pm 0.149$; $g_{\text{bar}} + e_N : 0.912 \pm 0.152$ and $g_{\text{bar}} + r : 0.920 \pm 0.163$.

($\alpha = 2, \beta = 1$), jerk J_{obs} ($\alpha = 3, \beta = 2$) and higher derivatives, without privileging any combination of V_{obs} and r . The full 2D parameter space of α, β need not be considered because $\mathcal{D}(\alpha, \beta)^\gamma$ is equally predictable as $\mathcal{D}(\alpha, \beta)$. Without loss of generality we therefore parametrize \mathcal{D} by a new variable $\theta \in [0, \pi)$, defined by

$$\tan \theta \equiv \frac{\beta}{\alpha}. \quad (17)$$

We consider individual baryonic properties, pairs of properties, and the full set of properties as predictors. The uncertainty in V_{obs} , D and i is propagated to $\mathcal{D}(\alpha, \beta)$ via

$$\frac{\delta \mathcal{D}(\alpha, \beta)}{\mathcal{D}(\alpha, \beta)} = \sqrt{\alpha^2 \frac{\delta V_{\text{obs}}^2}{V_{\text{obs}}^2} + \alpha^2 \frac{\delta i^2}{\tan^2 i} + \beta^2 \frac{\delta D^2}{D^2}}. \quad (18)$$

We generate the mock RAR-like data for an arbitrary θ following the approach of Section 3.5 as $\mathcal{D}(\alpha, \beta) = g_{\text{obs}}^{\alpha/2} r^{\alpha/2 - \beta}$, with g_{obs} computed using the RAR IF with $a_0 = 1.118 \times 10^{-10} \text{ ms}^{-2}$. This introduces an explicit correlation only between g_{bar} and g_{obs} . We similarly calculate \mathcal{D} for our mock data by calculating V_{obs} from either g_{obs} or J_{obs} and applying Eq. (16). This will let us determine the extent to which SPARC-like data with dynamics set solely by the $g_{\text{bar}} - g_{\text{obs}}$ or $\Sigma_{\text{tot}} - J_{\text{obs}}$ relation is able to match the predictivity of \mathcal{D} from baryonic variables in the real data.

We use the ET and NN regressors. For ET, we simplify the process by neglecting the propagation of uncertainty in the dependent variable and only generate sample weights using Eq. (18), showing the loss \mathcal{L}_0 . The ET hyperparameters are fixed to those used in the g_{obs} regression. For the NN, we fully incorporate the uncertainty in the dependent variables in the loss \mathcal{L} given by Eq. (9) and adopt the NN architecture and training described in Section 3.3.1.

We present the goodness-of-prediction of $\mathcal{D}(\alpha, \beta)$ by various features according to the ET model in Fig. 7. We compute \mathcal{L}_0 as a function of θ for individual features listed in Table 1 and for all features combined, showing the results for the real data in solid lines. We focus on the individual dependence of g_{bar} , Σ_{tot} , $L_{3.6}$, as the remaining features are either non-informative or exhibit no interesting trends. We find that g_{bar} is the best predictor of g_{obs} ($\theta = \arctan 1/2$), in agreement with the results of Section 4.1. Interestingly, we find that $L_{3.6}$ is the best predictor of V_{obs} . This is reminiscent of the TFR but surprising because $L_{3.6}$ is a galaxy-wide feature, which cannot therefore capture variations in V_{obs} within a single galaxy. Σ_{tot} is as good a predictor of $J_{\text{obs}} = V_{\text{obs}}^3/r^2$ as g_{bar} , and J_{obs} is approximately the dynamical quantity most predictable from Σ_{tot} . That the $J_{\text{obs}} - \Sigma_{\text{tot}}$ relation is the second strongest correlation in the data is what motivates our decision to investigate mock data created from it, as a foil for the RAR results. This is discussed further in Section 5.1.

The inclusion of additional features does not enhance the prediction of g_{obs} , corroborating the results of Section 4.1. Nevertheless, when considering all features simultaneously there is an improvement in predicting \mathcal{D} at $\theta \gtrsim \arctan(1/2)$ (black line) where the loss is as low as at g_{obs} . In fact, at the global minimum corresponding to $\tan \theta \approx 0.62$ the loss \mathcal{L}_0 per observation is lower by ~ 0.05 than the $g_{\text{bar}} - g_{\text{obs}}$ relation (i.e. the RAR). However, the 1σ Monte Carlo uncertainties of the loss are approximately ~ 0.34 and 0.26 for the minimum of the black line and the RAR, respectively, showing that the improvement is statistically insignificant. We also show the predictability of $\mathcal{D}(\theta)$ using g_{bar} , Σ_{tot} and then with g_{bar} , Σ_{tot} , M_{HI} . We observe that the addition of M_{HI} significantly reduces the loss, even though it is not informative by itself.

The dashed and dotted lines in Fig. 7 show analogous results obtained from the RAR and $\Sigma_{\text{tot}} - J_{\text{obs}}$ mock data, respectively (see Section 3.5). The mock RAR lines are remarkably consistent with the real data, showing that the RAR alone is approximately able to account for all dynamical correlations present in SPARC. Minor discrepancies arise in the case of predicting V_{obs} from $L_{3.6}$ at $\theta \sim 0$ and g_{obs} from g_{bar} . In the former, a stronger relation is found in the real data compared to the mock data, while in the latter, the relation is stronger in the mock data. These deviations are significant at less than the $\sim 2\sigma$ level given the formal uncertainties derived from the test-train splitting. However, we do not expect the mock data generation to encapsulate all nuances of real galaxies: the improved prediction at g_{obs} can be attributed to the absence of intrinsic scatter in the mock RAR data. We evaluate the root-mean-square (RMS) deviation of $\log g_{\text{obs}}$ from the RAR IF fit with respect to both the SPARC data and RAR IF mocks, obtaining values of ~ 0.133 and 0.128 dex, respectively. In mocks, this originates from accounting for the systematic uncertainties associated with Υ_{bulge} , Υ_{disk} , Υ_{gas} , i , D and $L_{3.6}$, as well as statistical uncertainty of V_{obs} (see Section 3.5). If we include a statistically independent intrinsic scatter its best-fit value is therefore ~ 0.034 dex, which agrees perfectly with that estimated by the more sophisticated analysis of Desmond (2023). Other discrepancies may be due to minor systematics in the data such as variations in disk thickness, inclination or mass-to-light ratios across the galaxies.

In contrast, the mock $\Sigma_{\text{tot}} - J_{\text{obs}}$ data does not accurately

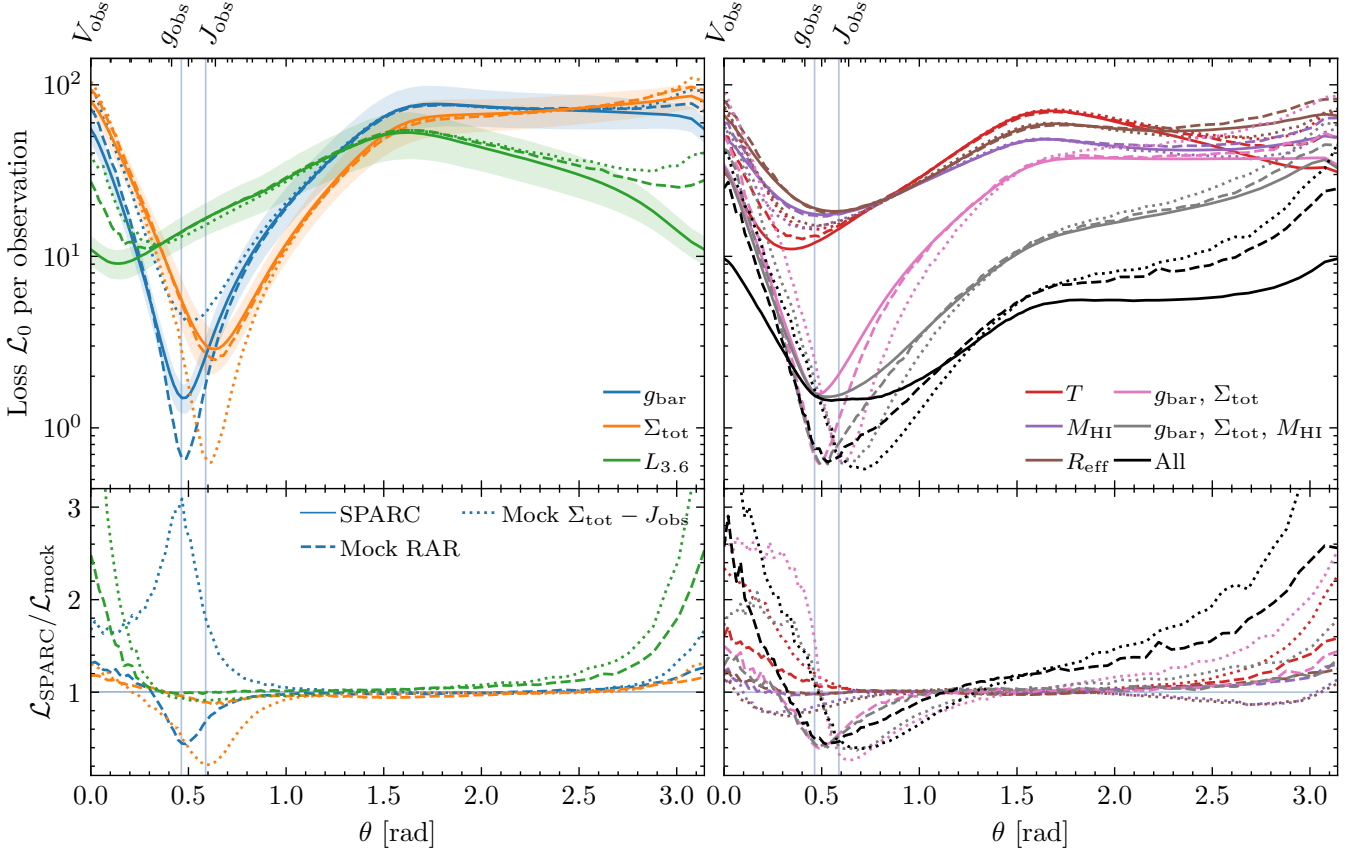


Figure 7. Averaged test set loss \mathcal{L}_0 for predicting $\mathcal{D}(\alpha, \beta) = V_{\text{obs}}^\alpha / r^\beta$ from individual or combinations of features using the ET regressor. The generic dynamical variable \mathcal{D} is parametrized by $\tan \theta \equiv \beta/\alpha$. Solid lines show the results in the SPARC data set, while dashed and dotted correspond to the mock RAR and $\Sigma_{\text{tot}} - J_{\text{obs}}$ data respectively. *Left panels:* g_{bar} , Σ_{tot} and $L_{3.6}$ used individually as predictors, with shaded regions indicating 1σ SPARC uncertainty. For clarity, we omit uncertainty bands for the mock data which are similar to those of the real data. *Right panels:* predictivity of other features individually and combinations of features (uncertainty bands omitted). The *lower panels* show the ratios of the SPARC and mock-evaluated losses. The RAR is the single strongest 1D relation between galaxy baryonic and dynamical properties, and the mock data using it accounts for the remaining SPARC correlations which therefore appear as nothing but aspects of the RAR. On the other hand, the mock $\Sigma_{\text{tot}} - J_{\text{obs}}$ mock data fails to explain the RAR as well as other observed dynamical correlations.

reproduce the dynamical SPARC correlations. Most notably, the RAR shows a much larger loss when predicting \mathcal{D} from g_{bar} , compared to the mock RAR data set which captures the $\Sigma_{\text{tot}} - J_{\text{obs}}$ correlation with a loss comparable to that of SPARC. It can also be seen that the $\Sigma_{\text{tot}} - J_{\text{obs}}$ mock has behaviour discrepant with SPARC when predicting from $L_{3.6}$. We verify that the agreement between SPARC and the RAR mock, and disagreement with the $\Sigma_{\text{tot}} - J_{\text{obs}}$ mock, extends also to features not shown in Fig. 7.

We present the corresponding ET relative permutation importances of g_{bar} , Σ_{tot} , $L_{3.6}$, M_{HI} , and T in Fig. 8. This quantifies the average increase of \mathcal{L}_0 per observation when a feature is permuted, normalized such that the sum of all importances is unity at each θ . These five features account for the majority of the ET-inferred importance. In the real data we observe a weak importance of galaxy type around V_{obs} , while at g_{obs} the ET recognizes g_{bar} as clearly the most important feature despite its strong correlation with Σ_{tot} . In case of J_{obs} , we see the permutation score to be significant for both g_{bar} and Σ_{tot} , however from Fig. 7 we know that the dependence of J_{obs} on Σ_{tot} is a consequence of the RAR

and, therefore, this is again just a case of g_{bar} and Σ_{tot} being strongly correlated. The dashed and dotted lines again show the permutation importances for the mock RAR and $\Sigma_{\text{tot}} - J_{\text{obs}}$ data respectively. While the former are again in agreement with the real data, the importance of g_{bar} and Σ_{tot} in the $\Sigma_{\text{tot}} - J_{\text{obs}}$ mocks disagrees strongly. This shows that the $\Sigma_{\text{tot}} - J_{\text{obs}}$ relation is a reflection of the RAR, not the other way around. Qualitatively similar conclusions hold for the decision tree importance scores calculated as the average impurity decrease due to a feature.

We repeat this analysis with the NN regressor, optimizing the loss \mathcal{L} . We focus only on the most important features— g_{bar} , Σ_{tot} , and $L_{3.6}$ —due to the increased computational cost associated with training the NN. This plot is not shown because despite the use of a different loss function, we observe almost identical trends to the ET analysis (Fig. 7). This shows that the results are not sensitive to the regressor used. Finally, to crosscheck the ML models’ findings we calculate the Kendall correlation coefficient of $\mathcal{D}(\alpha, \beta)$ with g_{bar} , Σ_{tot} , $L_{3.6}$, T , M_{HI} and R_{eff} Fig. 9. We again find that the strongest dynamical-to-baryonic correlation is between

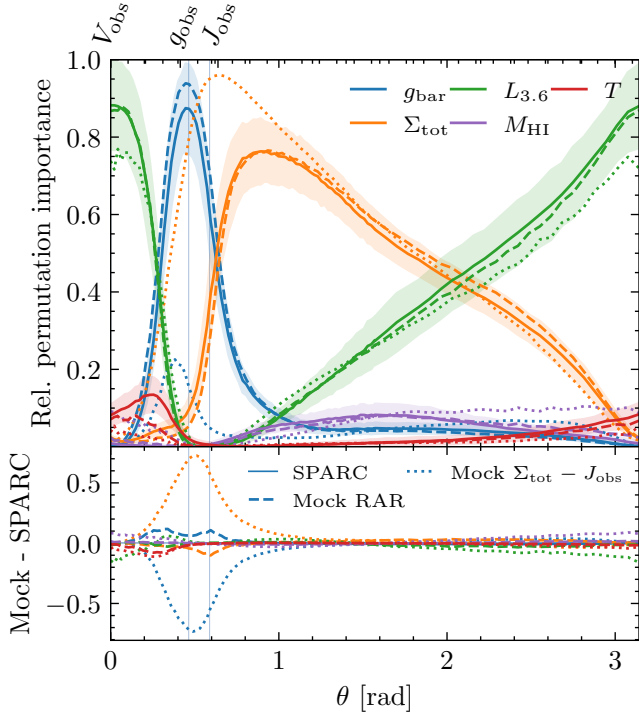


Figure 8. Relative permutation importances of selected features for predicting $\mathcal{D}(\alpha, \beta)$ using the ET regressor. Solid lines denote SPARC data (with 1σ uncertainty bands), while the dashed and dotted lines indicate the mock RAR and mock $\Sigma_{\text{tot}} - J_{\text{obs}}$ data, respectively. The lower panel shows the difference between the mock and SPARC importances. The shown features account for practically all of the model’s predictivity at all θ . As in Fig. 7, the consistency between the real and mock data shows that the relative importances of all features derive from the RAR in conjunction with the non-dynamical correlations present in SPARC.

g_{bar} and g_{obs} , with strong consistency between the real and RAR mock data. Again as in the ET analysis, the mock $\Sigma_{\text{tot}} - J_{\text{obs}}$ data fails to explain the dynamical correlations of SPARC: it predicts too strong a $\Sigma_{\text{tot}} - J_{\text{obs}}$ relation, and too weak a $g_{\text{obs}} - g_{\text{bar}}$, $L_{3.6} - V_{\text{obs}}$ and $T - V_{\text{obs}}$ relation. Scatter in the mock data or additional noise or systematics will only weaken these trends further in the mock data. By contrast, the mock RAR data recovers the $\Sigma_{\text{tot}} - J_{\text{obs}}$ relation (indeed the full $\Sigma_{\text{tot}} - \mathcal{D}$ relation) near-perfectly.

5 DISCUSSION

5.1 Implications of results

We demonstrate that in the SPARC sample the RAR is both necessary and sufficient to account for the full set of correlations among galaxy properties involving dynamical variables, so that it may be considered the fundamental relation of late-type galaxy dynamics. The fact that our ML regressors are unable to produce superior fits to the $g_{\text{bar}} - g_{\text{obs}}$ relation than the simple analytic expressions further testifies to the relative simplicity of the SPARC RAR, the information in which is almost fully captured by simple 1-2 parameter functions. Consequently, the primary task in comprehending these galaxies’ dynamics lies in understanding the emergence of the RAR

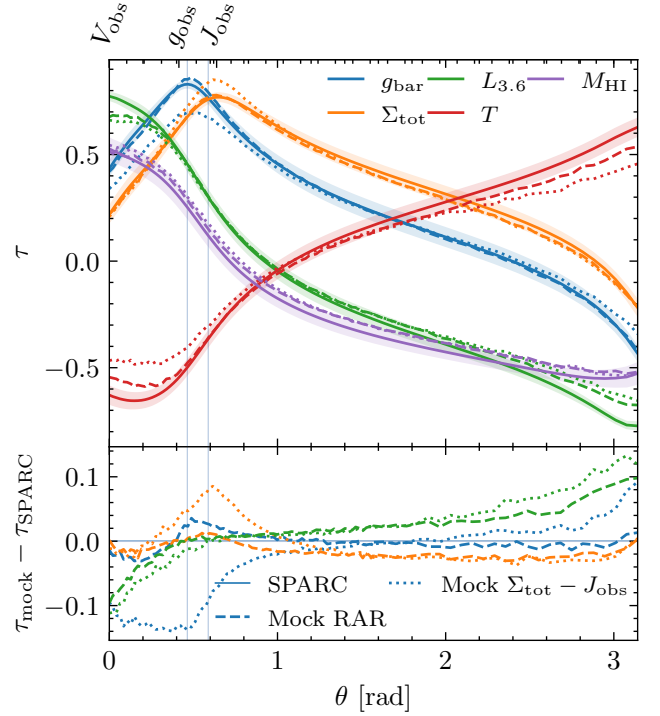


Figure 9. Kendall’s τ correlation coefficient between $\mathcal{D}(\alpha, \beta)$ and g_{bar} , Σ_{tot} , $L_{3.6}$, T , M_{HI} . Solid lines represent the SPARC data, dashed lines the mock RAR data, dotted lines the mock $\Sigma_{\text{tot}} - J_{\text{obs}}$ data and bands the 1σ SPARC uncertainties. The lower panel shows the difference between the mock and SPARC correlation coefficients, illustrating the superiority of the RAR mock data. The results corroborate and reinforce those of Figs. 7 and 8.

and non-emergence of any alternative or additional correlation.

While the RAR is an immediate consequence of MOND (Milgrom 1983a), its status in a Λ CDM cosmology is debated. Several authors argue that aspects of the RAR are highly challenging to reproduce in a Λ CDM-based galaxy formation scenario (Wu & Kroupa 2015; Desmond 2017; Tenetti et al. 2018; McGaugh 2015), while others argue that it emerges more or less naturally in hydrodynamical simulations or semi-analytic models (van den Bosch & Dalcanton 2000; Keller & Wadsley 2017; Ludlow et al. 2017). Even if the latter were so, the discovery that the RAR is apparently *the only* fundamental correlation of late-type galaxy dynamics provides an additional hurdle for such models. This adds to the existing challenges faced by Λ CDM models attempting to explain the RAR (Di Cintio & Lelli 2016; Desmond 2017; Keller & Wadsley 2017; Ludlow et al. 2017; Paranjape & Sheth 2021; Desmond 2023).

In Section 4.2, we showed that $L_{3.6}$ is individually the best predictor of V_{obs} , as expected from the TFR (Tully & Fisher 1977; McGaugh et al. 2000). This result was replicated using mock RAR data, indicating that the TFR-like $V_{\text{obs}} - L_{3.6}$ relation can be derived from the RAR. It is important to note however that V_{obs} is a local quantity, varying across a single galaxy’s RC, while the TFR is defined in terms of an overall characteristic velocity. The correlation is strongest when using the flat rotation velocity (Ponomareva et al. 2017, 2018; Lelli et al. 2019), which is only captured in the final V_{obs} val-

ues of some SPARC galaxies. It is therefore unsurprising that the $V_{\text{obs}} - L_{3.6}$ relation we find is significantly weaker than the true TFR. Additionally, we found that J_{obs} is well predictable individually by both g_{bar} and Σ_{tot} (which are strongly correlated as the former is calculated from the latter), with the $\Sigma_{\text{tot}} - J_{\text{obs}}$ correlation being a reflection of the RAR. We demonstrated that the $\Sigma_{\text{tot}} - J_{\text{obs}}$ correlation alone is insufficient to replicate the dynamical correlations in SPARC: it fails to accurately reproduce the observed RAR, while the RAR completely explains the observed $\Sigma_{\text{tot}} - J_{\text{obs}}$ relation. Additionally, its residuals are correlated with baryonic properties in the data, and if it were the correlation driving the dynamics it would induce residual correlations in the RAR, which are not observed.

We hypothesize that the $\Sigma_{\text{tot}} - J_{\text{obs}}$ correlation is caused by the specific disk matter distribution of SPARC galaxies, in conjunction with the RAR determining the dynamics. To test this, we calculate g_{bar} for model galaxies using (1) a thin exponential density profile (Mo et al. 2010, Eq. 11.30), and (2) the Kuzmin disk (Kuzmin 1956; Binney & Tremaine 2008, Eq. 2.68a) for the baryonic mass distribution. We then calculate g_{obs} and hence $\mathcal{D}(\theta)$ from the RAR IF. In both cases, we observe a maximum correlation between $\mathcal{D}(\theta)$ and surface brightness around $\theta = \arctan(2/3)$, i.e. J_{obs} , as in the real data, although the correlation of the disk solution peaks closer to $\theta = \arctan(1/2)$, i.e. g_{obs} . This shows that the fact that the $\Sigma_{\text{tot}} - \mathcal{D}$ relation peaks almost exactly at J_{obs} in SPARC is somewhat coincidental because it depends on the baryonic mass profile; for a different sample the extrema of \mathcal{L}_0 and τ may occur at a θ different by some tenths of a radian.

We assumed that both the RAR and $\Sigma_{\text{tot}} - J_{\text{obs}}$ relations have no intrinsic scatter when generating the mock data. While this assumption is approximately true for the RAR (Desmond 2023 measured it to be 0.034 ± 0.002 dex), it is unlikely to hold for $\Sigma_{\text{tot}} - J_{\text{obs}}$. However, adding uncorrelated intrinsic scatter to the latter relation can only weaken the correlations, deteriorating the prediction of the RAR still further. While it is possible to introduce correlations of the residuals with other variables and fine-tune them to reproduce the correlations seen in the data, this will simply approximate the success of the mock data generated solely according to the RAR. Thus the RAR satisfies the fundamentality criterion of Section 1 that it can explain the other dynamical correlations, while the $\Sigma_{\text{tot}} - J_{\text{obs}}$ relation does not. Since that relation is the second strongest 1-dimensional correlation in the data (measured by \mathcal{L}_0 , \mathcal{L} or τ), it follows that no dynamical correlation in the SPARC data set besides the RAR can be fundamental: the rest will make even worse predictions for the RAR and $\mathcal{D}(\theta)$ generally.

Within the MOND paradigm our analysis is capable of shedding light on the presence or absence of the EFE. We confirm previous results (Haghi et al. 2016; Chae et al. 2020b, 2021, 2022; Desmond 2023) that the inclusion of the EFE improves the fit to galaxy kinematics (i.e. the Simple IF + EFE relative to the RAR IF), and show that the largest partial correlation of g_{obs} at fixed g_{bar} is with the external field strength e_N (Fig. 2). This suggests the external field to be the most important quantity besides g_{bar} in the determination of g_{obs} . However, when performing test-train splits the Simple IF + EFE no longer outperforms the RAR IF (Fig. 5), and none of our regressors can utilize e_N to improve the pre-

diction of g_{obs} (shown for the ET regressor in Fig. 6). We therefore do not find significant evidence for the EFE, and conclude that better data is required to establish the validity or breakdown of the strong equivalence principle in galaxy RCs. This conclusion agrees with Paranjape & Sheth (2022), who challenge the EFE detection of Chae et al. (2021) on the basis of large RC uncertainties and potential inaccuracies in estimating the external field strength. Moreover, they argue that Λ CDM naturally predicts an EFE-like correlation, albeit with an opposite sign to that of MOND.

5.2 Caveats and systematic uncertainties

5.2.1 Scope of the conclusions

As mentioned at the end of Section 1, it is important to stress that our results on the fundamentality of the RAR do not extend to late-type galaxy dynamics *in their totality*, but only to *equilibrium radial* dynamics. The RAR is limited to motion in the plane of the disk and does not cover the perpendicular, vertical motion which also possesses much interesting dynamics. Examples include vertical velocity dispersion in disks (e.g. van der Kruit & Freeman 1984; Bershadsky et al. 2010), vertical “breathing modes” (e.g. Kumar et al. 2022; Ghosh et al. 2022) and the more complicated anisotropic motions of bars and bulges. There also exist dynamical scaling relations in late-type galaxies that involve the vertical gravitational field such as the central baryonic–dynamical surface density relation (Lelli et al. 2016c). The perpendicular structure of the disk is important for phenomena such as the “Freeman law,” an observed upper limit to disk surface densities (Freeman 1970; Bosma & Freeman 1993; McGaugh et al. 1995), which may arise from stability requirements involving the full 3D structure (Banik et al. 2018). Out-of-equilibrium and non-axisymmetric dynamics cause deviations from the regular radial motions encapsulated by the RAR and are therefore also not covered by our analysis.

The other important restriction to the scope of our conclusion, even within the radial dynamics of late-types, is that the RAR is not a substitute for the galaxy-by-galaxy study of RCs. Our conclusions therefore only hold for equilibrium radial dynamics when stacked across many galaxies and viewed statistically, i.e. *on average*. Although the RAR contains the correlation of the RCs with the baryonic mass distribution, particular points may be of special interest without standing out in the RAR plane. An example is “Renzo’s rule,” a point-by-point correlation of features in the baryonic mass profile with features of the RCs (Sancisi 2004; Famaey & McGaugh 2012). While obvious in case the baryons dominate the mass budget, this is difficult to understand in Λ CDM if the RC is dominated by the dark matter as this is supposed to be featureless and uncorrelated with the baryons. Velocity measurements for which this is pronounced are rare, so a model may predict the statistics of the RAR successfully on average while completely missing this behaviour: it would introduce only a few, relatively small residuals. Thus it cannot be said that explaining the RAR alone is sufficient to account in full generality for late-type galaxy dynamics, but only for the average equilibrium radial dynamics, parametrized by \mathcal{D} , that we have studied here.

5.2.2 Goodness-of-fit & model complexity

Fig. 5 shows that while our NN performs comparably to the RAR IF and Simple IF + EFE, the losses achieved by the ET and XGB regressors are systematically higher. This is intriguing, given that the ML models are nearly arbitrarily complex and hence should be able to fit the data better. The suboptimal performance of the ML models could potentially be attributed to three factors: (1) the sampling of the underlying RAR distribution in SPARC, (2) overfitting and imperfect hyperparameter optimization, and/or (3) edge effects. We discuss each of these in turn.

First, the samples on the $g_{\text{bar}} - g_{\text{obs}}$ plane are not independent and identically distributed, but instead are strongly correlated within each galaxy. Coupled with the relatively small sample size, this may result in inadequate representation of the test set by the training set galaxies, leading to suboptimal performance of the ET and XGB models. These models can only interpolate discontinuously between past observations, whereas the analytic functions, constrained by their functional form, and NN, which smoothly interpolates between past observations, are more robust in this regard. When training and evaluating the ML regressors on all data (i.e., without a test-train split), they “outperform” the analytic functions due to overfitting.

Second, as depicted in the lower panel of Fig. 4, the XGB and ET models generate a markedly jagged fit, suggesting potential overfitting on training samples. Enhancing the generalization capability of ML models often involves hyperparameters optimization, a crucial aspect of our analysis. We employed an automatic hyperparameter optimization using *Optuna*, conducting the optimization on the full training data until convergence and selecting hyperparameter that minimize the loss on validation samples selected via cross-validation. The choice of the number of folds is crucial as it determines the balance between training and validation; both extremes may lead to a non-representative validation loss. We opted for 5-fold cross-validation to optimize the hyperparameters, although the goodness-of-fit was similar when using either 3- or 4-fold cross-validation instead. The prime method of reducing overfitting is to reduce the complexity of the regressors, for example by restricting the maximum depth of decision trees or the minimum number of samples required to split a node. Although these are already optimized by *Optuna* (see Table 2), it is possible that a further small improvement could be achieved by hand-tuning them. Indeed the complexity threshold before overfitting occurs appears to be very low on the RAR data: as shown in Fig. 5, the Simple IF + EFE fits the entire SPARC data set better than the RAR IF but worse when train-test splitting is implemented. This function with only two free parameters is therefore likely overfitted.

Third, in Fig. 4 the performance of the ET and XGB models deteriorates near the boundaries of the data set, where the average loss per point is higher than average. This limitation arises from the decision trees’ inability to extrapolate beyond past observations, resulting in predictions biased towards the mean. The impact of this on the loss distribution is, however, on the order of a few per cent, and is therefore not the main cause of the poor performance of the ET and XGB regressors.

5.2.3 Neural network convergence

Although our NN allows derivatives to be propagated fully into the loss function and achieves as high accuracy as the RAR IF, it is not without problems. Despite extensive training, convergence to a global minimum of the loss is in practice not guaranteed due to the high dimensionality of the parameter space of the NN weights and biases. Indeed, whether an NN has converged to the global minimum is generally unclear. One way to address this is to use an ensemble of NNs, where the predictions are stacked to quantify the predictive disagreement arising purely from training (Stiskalek et al. 2022). An alternative approach to enhance the accuracy and generalizability is to incorporate additional information (“physics”) during training to create a “physics-informed neural network” (PINN; Karniadakis et al. 2021; Cuomo et al. 2022). This may involve modification to the network architecture, loss function and/or activation functions. This however comes at the cost of reducing the agnosticism and purely empirical nature of the NN, and the simple exercise of replacing the linear connection of the input and output layer in our NN with the RAR IF (optimizing a_0 alongside the other NN parameters) produced no improvement relative to the RAR IF alone. This again supports the conclusion that residuals of the RAR around the RAR IF are devoid of physical information.

5.2.4 Raw data reduction & SPARC selection

The SPARC data contains various systematics unaccounted for in our mock data or likelihood model. This includes inclination variations across the disks in the tilted ring fits, potential variations in mass-to-light ratios and disk thickness across the RC and other assumptions made about the structure of the baryonic mass when solving for the RC such as the vertical distribution of the gas density (Di Teodoro & Fraternali 2015). However, Mancera Piña et al. (2022) demonstrated that gas disk flaring is only important for halo properties inferred from RC fitting in the smallest, gas-dominated dwarf galaxies. The data is also selected inhomogeneously, based on the high-quality RCs that happen to have been derived in the literature. Nevertheless, SPARC provides a thorough sampling of the physical parameter space occupied by rotationally supported galaxies, and there is no obvious reason to expect systematics or selection to bias our results. Some suggestions for the more sophisticated modelling required to corroborate our conclusions with greater precision are given below.

5.3 Suggestions for further work

5.3.1 Increasing the robustness of the inference

Our likelihood functions Eqs. (9) and (11) assume that all of the points on the RAR are independent. This is not true in detail because the methods used to derive the RC of a given galaxy necessarily couple the points, and several of the parameters relevant to V_{obs} and V_{bar} —distance, inclination and mass-to-light ratios—are properties of the galaxies as a whole. It is possible to infer these parameters simultaneously with a fit to the RAR (Desmond 2023), but this assumes a functional form for the fit and hence is not useful for our

more agnostic analysis here. It would however be possible to construct a covariance matrix for g_{obs} and g_{bar} within each galaxy by Monte Carlo-sampling D , i and Υ_X and use that in the Gaussian likelihood, thus assuming that galaxies are independent while RC points for a given galaxy are not.

A truly irreproachable demonstration of the fundamentality of the RAR would require showing that its residuals correlate with *no* other galaxy or environment property. Here we are restricted to features present in the SPARC data set plus e_N as calculated in [Chae et al. \(2021\)](#). Other interesting features could include colour, star formation rate and environmental density (or functions thereof) on a range of scales, which could be acquired by cross-correlating SPARC with other surveys and repeating the calculations of [Chae et al. \(2021\)](#) for other environmental measures. As an example, $\sim 2/3$ of the SPARC galaxies were observed in the SDSS and hence possess all properties derivable from that survey.

Our “generic dynamical variable” adopts the specific functional form $\mathcal{D}(\alpha, \beta) = V_{\text{obs}}^\alpha / r^\beta$, allowing it to be fully parameterized by an angle $\theta = \arctan(\beta/\alpha)$. This choice is motivated by the fact that it encompasses all time derivatives of uniform circular motion—velocity, acceleration, jerk and higher—while offering a seamless interpolation between them. While one might consider parameterizing the dynamical space using a more intricate function, dimensional analysis alone imposes significant constraints. For instance, a linear combination of terms like \mathcal{D} would require the addition of dimensionful coefficients, increasing complexity and difficulty of interpretation while limiting generalizability. A parallel argument applies to e.g. trigonometric functions or exponentials: their arguments must be dimensionless, necessitating a dimensionful constant to remove the dimensions of V_{obs} and r . Thus, while other dynamical variables could be possible, their further consideration is beyond the scope of this work.

There exists a range of $\tan \theta > 1/2$ over which \mathcal{D} can be predicted equally well from several features (g_{bar} , Σ_{tot} , D , i , $L_{3.6}$, M_{HI} , T , R_{eff} , and e_N). Our conservative primary conclusion is therefore that the RAR represents the optimal *1-dimensional* correlation between baryonic and dynamical properties. For all intents and purposes it is the optimal correlation of any dimension also, as the improvement observed in Fig. 7 when using many features is statistically insignificant. While we cannot rule out the existence of a feature set that enhances predictivity of \mathcal{D} beyond that of the RAR, such evidence is not found in SPARC.

Our analysis is not tied to a specific functional form for the RAR: to benchmark the ML regressor results we have employed the RAR IF and Simple IF + EFE simply as example $g_{\text{bar}} - g_{\text{obs}}$ relations that are known to fit the data reasonably well. This is fortunate, as [Desmond et al. \(2023\)](#) demonstrated using symbolic regression that there exist more accurate and simpler functions than these. Utilizing the optimal functions from [Desmond et al.](#) would reduce the loss of the $g_{\text{bar}} - g_{\text{obs}}$ relation, but would not alter the conclusion that incorporating additional features does not improve accuracy. However, given the greater success of symbolic regression than numerical ML methods it would be interesting to try to construct multi-variable symbolic fits for g_{obs} using all available features. This would likely be less prone to overfitting when using an information-theoretic model selection criterion such as the minimum description length principle ([Bartlett et al. 2022](#)), and to confusion when irrelevant features are

considered. Feature importance may be assessed by the frequency of occurrence of variables in highly-ranked functions, or by the difference in accuracy or description length between similar functions including or not including a variable. While currently beyond the complexity limit of Exhaustive Symbolic Regression ([Bartlett et al. 2022](#)), this could be achieved by genetic algorithms such as OPERON ([Burlacu et al. 2020](#)).

5.3.2 Additional data

We have selected the SPARC sample as representative of the late-type galaxy population, given its extensive range in morphology (S0 to Irr), luminosity and surface brightness, and unrestrictive selection criteria ([Lelli et al. 2016a](#)). To assess the impact of sample variance, we employed test-train splitting (a form of jackknifing) and Monte Carlo mock data generation, showing that our findings would be applicable to all SPARC-like data realizations. However, to establish the RAR as the fundamental dynamical correlation for late-type galaxies in general, further analysis on alternative data sets, such as LITTLE THINGS ([Iorio et al. 2017](#)) or PROBES ([Stone et al. 2022](#)), is necessary. Although these larger data sets may yield increased statistical uncertainties due to lower quality requirements, the same conclusions should be reached if the error model is reliable.

Ideally, the results presented here would be generalized further to the dynamics of galaxies of all types. The RAR has been investigated in diverse contexts, such as ultra-diffuse galaxies (e.g. [Freundlich et al. 2022](#)), local dwarf spheroidals (e.g. [McGaugh & Wolf 2010](#); [McGaugh & Milgrom 2013](#)), low-acceleration regions including the outer Milky Way ([Oman et al. 2020](#)), early-type galaxies ([Lelli et al. 2017](#); [Shelest & Lelli 2020](#); [Chae et al. 2019, 2020a](#); [Tian & Ko 2017](#)) and galaxy groups and clusters ([Chan & Del Popolo 2020](#); [Tian et al. 2020](#); [Pradyumna & Desai 2021](#); [Gopika & Desai 2021](#)). Although these data sets contain sufficient information for our analysis, the properties employed as features may differ, and additional systematic uncertainties may arise. However, given that the SPARC galaxies are not qualitatively different to others—and are related to them evolutionarily—one would expect conclusions concerning the fundamentality of the RAR to generalize. Exploring the RAR using qualitatively different observables, such as stacked weak lensing ([Brouwer et al. 2021](#)), could provide valuable consistency checks and extend our results to new regimes.

5.3.3 Testing Λ CDM

It would be interesting to perform our analysis on mock data generated by Λ CDM (through a semi-analytic model and/or hydrodynamical simulation), to see if, as in the data, g_{obs} is uniquely predictable from g_{bar} , $\{\alpha = 2, r = 1\}$ locates the $V_{\text{obs}}^\alpha / r^\beta$ most strongly correlated with baryonic properties and the $g_{\text{bar}} - g_{\text{obs}}$ relation accounts for all dynamical correlations. It seems these would be unlikely coincidences, as neither g_{bar} nor g_{obs} have any particular significance in that theory.

6 CONCLUSION

We explore the origin of galaxies' surprising simplicity by studying the radial acceleration relation (RAR), which generalizes and subsumes the statistical regularities of late-type galaxies' radial (in-disk) dynamics. In particular, we question whether the RAR is *the fundamental* relation of late-type radial dynamics, by which we mean that

- (i) its residuals do not correlate significantly with any other quantity,
- (ii) it is the strongest dynamical-to-baryonic correlation,
- (iii) it is sufficient to explain all other correlations involving radial dynamics (in conjunction with the non-dynamical correlations of the data set we use), and
- (iv) no other relation possesses these properties.

To do so we develop machine learning regressors for predicting dynamic variables from baryonic ones, establishing feature importance directly and by determining which variables contribute usefully to the prediction. We supplement this by a partial correlation analysis of RAR residuals and validate our results on mock data that matches the non-dynamical properties of the Spitzer Photometry & Accurate Rotation Curves (SPARC) data while allowing control of its kinematic correlations.

We find the RAR to satisfy all of these criteria for unique fundamentality: features besides g_{bar} only degrade the prediction of g_{obs} (which in fact cannot significantly exceed simple fitting functions in accuracy), predicting a general dynamical variable $V_{\text{obs}}^\alpha/r^\beta$ picks out $\{\alpha = 2, r = 1\}$, i.e. g_{obs} , as the most predictable from baryonic features, and mock data including the RAR but no other dynamical correlation has all $\{\alpha, \beta\}$ correlations approximately consistent with the real data. Subsidiary correlations such as between luminosity and velocity or surface brightness and jerk are explicable as projections of the RAR, but not vice versa. Indeed, the second strongest 1-dimensional dynamical correlation in the data possesses *none* of the properties (i) - (iii) above. The RAR therefore appears to be the fundamental 1-dimensional correlation of late-type radial galaxy dynamics; consequently, to explain such dynamics it is necessary to explain the RAR, and sufficient to explain the RAR plus the lack of any other significant, partially independent correlation. This poses an extremely stringent test for theories of galaxy formation, which those based on modified dynamics readily pass while those based on concordance cosmology may not.

DATA AVAILABILITY

The SPARC data is available at <http://astroweb.cwru.edu/SPARC/>. The code underlying this article is available at <https://github.com/Richard-Sti/RARinterpret> and other data will be made available on reasonable request to the authors.

ACKNOWLEDGEMENTS

We thank Julien Devriendt, Harley Katz, Federico Lelli, Stacy McGaugh, Mordehai Milgrom, Adrienne Slyz and Tariq Yasin for useful comments and discussions. We also thank Jonathan Patterson for smoothly running the Glamdring

Cluster hosted by the University of Oxford, where the data processing was performed. RS acknowledges financial support from STFC Grant No. ST/X508664/1. HD is supported by a Royal Society University Research Fellowship (grant no. 211046). This project has received funding from the European Research Council (ERC) under the European Union's Horizon 2020 research and innovation programme (grant agreement No 693024). For the purpose of open access, we have applied a Creative Commons Attribution (CC BY) licence to any Author Accepted Manuscript version arising.

REFERENCES

- Abadi M., et al., 2015, TensorFlow: Large-Scale Machine Learning on Heterogeneous Systems, <https://www.tensorflow.org/>
- Akiba T., Sano S., Yanase T., Ohta T., Koyama M., 2019, arXiv e-prints, p. [arXiv:1907.10902](https://arxiv.org/abs/1907.10902)
- Asencio E., Banik I., Kroupa P., 2021, *MNRAS*, **500**, 5249
- Baba K., Shibata R., Sibuya M., 2004, *Australian & New Zealand Journal of Statistics*, **46**, 657
- Banik I., Milgrom M., Zhao H., 2018, arXiv e-prints, p. [arXiv:1808.10545](https://arxiv.org/abs/1808.10545)
- Bartlett D. J., Desmond H., Ferreira P. G., 2022, arXiv e-prints, p. [arXiv:2211.11461](https://arxiv.org/abs/2211.11461)
- Bekenstein J., Milgrom M., 1984, *ApJ*, **286**, 7
- Bender R., Burstein D., Faber S. M., 1992, *ApJ*, **399**, 462
- Berger J. O., Liseo B., Wolpert R. L., 1999, *Statistical Science*, **14**, 1
- Bershady M. A., Verheijen M. A. W., Swaters R. A., Andersen D. R., Westfall K. B., Martinsson T., 2010, *ApJ*, **716**, 198
- Binney J., Tremaine S., 2008, Galactic Dynamics: Second Edition, rev - revised, 2 edn. Princeton University Press, <http://www.jstor.org/stable/j.ctvc778ff>
- Bishop C. M., Nasrabadi N. M., 2007, *Journal of Electronic Imaging*, **16**, 049901
- Bosma A., Freeman K. C., 1993, *AJ*, **106**, 1394
- Bournaud F., 2010, *Advances in Astronomy*, 2010
- Breiman L., 2001, *Mach. Learn.*, **45**, 5–32
- Brosche P., 1973, *A&A*, **23**, 259
- Brouwer M. M., et al., 2021, *A&A*, **650**, A113
- Bujarrabal V., Guibert J., Balkowski C., 1981, *A&A*, **104**, 1
- Burlacu B., Kronberger G., Kommenda M., 2020, in Proceedings of the 2020 Genetic and Evolutionary Computation Conference Companion. GECCO '20. Association for Computing Machinery, New York, NY, USA, p. 1562–1570, doi:10.1145/3377929.3398099, <https://doi.org/10.1145/3377929.3398099>
- Cappellari M., et al., 2013, *MNRAS*, **432**, 1709
- Chae K.-H., Milgrom M., 2022, *ApJ*, **928**, 24
- Chae K.-H., Bernardi M., Sheth R. K., Gong I.-T., 2019, *ApJ*, **877**, 18
- Chae K.-H., Bernardi M., Domínguez Sánchez H., Sheth R. K., 2020a, *ApJ*, **903**, L31
- Chae K.-H., Lelli F., Desmond H., McGaugh S. S., Li P., Schombert J. M., 2020b, *ApJ*, **904**, 51
- Chae K.-H., Desmond H., Lelli F., McGaugh S. S., Schombert J. M., 2021, *ApJ*, **921**, 104
- Chae K.-H., Lelli F., Desmond H., McGaugh S. S., Schombert J. M., 2022, *Phys. Rev. D*, **106**, 103025
- Chan M. H., Del Popolo A., 2020, *MNRAS*, **492**, 5865
- Chang Y.-Y., Chao R., Wang W.-H., Chen P., 2010, arXiv e-prints, p. [arXiv:1009.0030](https://arxiv.org/abs/1009.0030)
- Chen T., Guestrin C., 2016, arXiv e-prints, p. [arXiv:1603.02754](https://arxiv.org/abs/1603.02754)
- Colwell D. J., Gillett J. R., 1982, *The Mathematical Gazette*, **66**, 307–309
- Conselice C. J., 2006, *MNRAS*, **373**, 1389

- Cooray S., Takeuchi T. T., Kashino D., Yoshida S. A., Ma H.-X., Kono K. T., 2022, [arXiv e-prints](#), p. [arXiv:2210.05862](#)
- Cuomo S., Schiano di Cola V., Giampaolo F., Rozza G., Raissi M., Piccialli F., 2022, [arXiv e-prints](#), p. [arXiv:2201.05624](#)
- Davidzon I., et al., 2022, *A&A*, **665**, A34
- Desmond H., 2017, *MNRAS*, **464**, 4160
- Desmond H., 2023, [arXiv e-prints](#), p. [arXiv:2303.11314](#)
- Desmond H., Wechsler R. H., 2017, *MNRAS*, **465**, 820
- Desmond H., Katz H., Lelli F., McGaugh S., 2019, *MNRAS*, **484**, 239
- Desmond H., Bartlett D. J., Ferreira P. G., 2023, [arXiv e-prints](#), p. [arXiv:2301.04368](#)
- Di Cintio A., Lelli F., 2016, *MNRAS*, **456**, L127
- Di Teodoro E. M., Fraternali F., 2015, *MNRAS*, **451**, 3021
- Disney M. J., Romano J. D., Garcia-Appadoo D. A., West A. A., Dalcanton J. J., Cortese L., 2008, *Nature*, **455**, 1082
- Djorgovski S., Davis M., 1987, *ApJ*, **313**, 59
- Dressler A., Lynden-Bell D., Burstein D., Davies R. L., Faber S. M., Terlevich R., Wegner G., 1987, *ApJ*, **313**, 42
- F.R.S. K. P., 1901, *The London, Edinburgh, and Dublin Philosophical Magazine and Journal of Science*, **2**, 559
- Famaey B., McGaugh S. S., 2012, *Living Reviews in Relativity*, **15**, 10
- Freeman K. C., 1970, *ApJ*, **160**, 811
- Freundlich J., Famaey B., Oria P.-A., Bílek M., Müller O., Ibata R., 2022, *A&A*, **658**, A26
- Friedman J. H., 2001, *The Annals of Statistics*, **29**, 1189
- Friedman J. H., 2002, *Computational Statistics & Data Analysis*, **38**, 367
- Gal Y., Ghahramani Z., 2015, [arXiv e-prints](#), p. [arXiv:1506.02142](#)
- Garcia-Appadoo D. A., West A. A., Dalcanton J. J., Cortese L., Disney M. J., 2009, *MNRAS*, **394**, 340
- Geurts P., Ernst D., Wehenkel L., 2006, *Machine Learning*, **36**, 3
- Ghosh S., Debattista V. P., Khachatryan T., 2022, *MNRAS*, **511**, 784
- Gopika K., Desai S., 2021, *Physics of the Dark Universe*, **33**, 100874
- Gunes Baydin A., Pearlmutter B. A., Andreyevich Radul A., Siskind J. M., 2015, [arXiv e-prints](#), p. [arXiv:1502.05767](#)
- Haghi H., Bazkiaei A. E., Zonoozi A. H., Kroupa P., 2016, *MNRAS*, **458**, 4172
- Hemmati S., et al., 2019, *ApJ*, **881**, L14
- Hotelling H., 1936, *Biometrika*, **28**, 321
- Iorio G., Fraternali F., Nipoti C., Di Teodoro E., Read J. I., Battaglia G., 2017, *MNRAS*, **466**, 4159
- Karniadakis G. E., Kevrekidis I. G., Lu L., Perdikaris P., Wang S., Yang L., 2021, *Nature Reviews Physics*, **3**, 422
- Keller B. W., Wadsley J. W., 2017, *ApJ*, **835**, L17
- Kendall M. G., 1938, *Biometrika*, **30**, 81
- Kingma D. P., Ba J., 2014, [arXiv e-prints](#), p. [arXiv:1412.6980](#)
- Kollmeier J. A., et al., 2017, [arXiv e-prints](#), p. [arXiv:1711.03234](#)
- Krishna S., Han T., Gu A., Pombra J., Jabbari S., Wu S., Lakkaraju H., 2022, [arXiv e-prints](#), p. [arXiv:2202.01602](#)
- Kumar A., Ghosh S., Kataria S. K., Das M., Debattista V. P., 2022, *MNRAS*, **516**, 1114
- Kuzmin G., 1956, *Astron. Zh.*, **33**, 27
- Lelli F., 2023, [arXiv e-prints](#), p. [arXiv:2305.18224](#)
- Lelli F., McGaugh S. S., Schombert J. M., 2016a, *AJ*, **152**, 157
- Lelli F., McGaugh S. S., Schombert J. M., 2016b, *ApJ*, **816**, L14
- Lelli F., McGaugh S. S., Schombert J. M., Pawlowski M. S., 2016c, *ApJ*, **827**, L19
- Lelli F., McGaugh S. S., Schombert J. M., Pawlowski M. S., 2017, *ApJ*, **836**, 152
- Lelli F., McGaugh S. S., Schombert J. M., Desmond H., Katz H., 2019, *MNRAS*, **484**, 3267
- Loshchilov I., Hutter F., 2016, [arXiv e-prints](#), p. [arXiv:1608.03983](#)
- Lovell C. C., Harrison I., Harikane Y., Tacchella S., Wilkins S. M., 2023, *MNRAS*, **518**, 2511
- Ludlow A. D., et al., 2017, *Phys. Rev. Lett.*, **118**, 161103
- Lundberg S., Lee S.-I., 2017, [arXiv e-prints](#), p. [arXiv:1705.07874](#)
- Lundberg S. M., et al., 2020, *Nature Machine Intelligence*, **2**, 56
- Mancera Piña P. E., et al., 2019, *ApJ*, **883**, L33
- Mancera Piña P. E., et al., 2020, *MNRAS*, **495**, 3636
- Mancera Piña P. E., Fraternali F., Oosterloo T., Adams E. A. K., di Teodoro E., Bacchini C., Iorio G., 2022, *MNRAS*, **514**, 3329
- McGaugh S. S., 2004, *ApJ*, **609**, 652
- McGaugh S. S., 2012, *AJ*, **143**, 40
- McGaugh S. S., 2015, *Canadian Journal of Physics*, **93**, 250
- McGaugh S., Milgrom M., 2013, *ApJ*, **775**, 139
- McGaugh S. S., Wolf J., 2010, *ApJ*, **722**, 248
- McGaugh S. S., Bothun G. D., Schombert J. M., 1995, *AJ*, **110**, 573
- McGaugh S. S., Schombert J. M., Bothun G. D., de Blok W. J. G., 2000, *ApJ*, **533**, L99
- Milgrom M., 1983a, *ApJ*, **270**, 365
- Milgrom M., 1983b, *ApJ*, **270**, 371
- Milgrom M., 1983c, *ApJ*, **270**, 384
- Mo H., van den Bosch F., White S., 2010, *Disk Galaxies*. Cambridge University Press, p. 495–543, doi:10.1017/CBO9780511807244.012
- Oman K. A., Brouwer M. M., Ludlow A. D., Navarro J. F., 2020, [arXiv e-prints](#), p. [arXiv:2006.06700](#)
- Paranjape A., Sheth R. K., 2021, *MNRAS*, **507**, 632
- Paranjape A., Sheth R. K., 2022, *MNRAS*, **517**, 130
- Pawlowski M. S., 2018, *Modern Physics Letters A*, **33**, 1830004
- Pedregosa F., et al., 2011, *Journal of Machine Learning Research*, **12**, 2825
- Pizagno J., et al., 2007, *AJ*, **134**, 945
- Ponomareva A. A., Verheijen M. A. W., Peletier R. F., Bosma A., 2017, *MNRAS*, **469**, 2387
- Ponomareva A. A., Verheijen M. A. W., Papastergis E., Bosma A., Peletier R. F., 2018, *MNRAS*, **474**, 4366
- Portillo S. K. N., Parejko J. K., Vergara J. R., Connolly A. J., 2020, *AJ*, **160**, 45
- Pradyumna S., Desai S., 2021, *Physics of the Dark Universe*, **33**, 100854
- Puth M.-T., Neuhauser M., Ruxton G. D., 2015, *Animal Behaviour*, **102**, 77
- Rahmani S., Teimoorinia H., Barmby P., 2018, *MNRAS*, **478**, 4416
- Rees M. J., Ostriker J. P., 1977, *MNRAS*, **179**, 541
- Roberts D. A., Yaida S., Hanin B., 2021, [arXiv e-prints](#), p. [arXiv:2106.10165](#)
- Rumelhart D. E., Hinton G. E., Williams R. J., 1986, *Nature*, **323**, 533
- Sancisi R., 2004, in *Ryder S., Pisano D., Walker M., Freeman K., eds*, Vol. 220, *Dark Matter in Galaxies*. p. 233 ([arXiv:astro-ph/0311348](#)), doi:10.48550/arXiv.astro-ph/0311348
- Sanders R. H., 1990, *A&ARv*, **2**, 1
- Shelest A., Lelli F., 2020, *A&A*, **641**, A31
- Stiskalek R., Bartlett D. J., Desmond H., Anbajagane D., 2022, *MNRAS*, **514**, 4026
- Stone C., Courteau S., Arora N., Frosst M., Jarrett T. H., 2022, *ApJS*, **262**, 33
- Tenneti A., Mao Y.-Y., Croft R. A. C., Di Matteo T., Kosowsky A., Zago F., Zentner A. R., 2018, *MNRAS*, **474**, 3125
- Tian Y., Ko C.-M., 2017, *MNRAS*, **472**, 765
- Tian Y., Umetsu K., Ko C.-M., Donahue M., Chiu I. N., 2020, *ApJ*, **896**, 70
- Tully R. B., Fisher J. R., 1977, *A&A*, **54**, 661
- Vanderplas J., Connolly A., 2009, *AJ*, **138**, 1365
- White S. D. M., Frenk C. S., 1991, *ApJ*, **379**, 52
- White S. D. M., Rees M. J., 1978, *MNRAS*, **183**, 341
- Whitmore B. C., 1984, *ApJ*, **278**, 61
- Wu X., Kroupa P., 2015, *MNRAS*, **446**, 330
- in der Au A., Meusinger H., Schallbach P. F., Newholm M., 2012, *A&A*, **547**, A115

van Dokkum P., et al., 2018, [Nature](#), **555**, 629

van den Bosch F. C., Dalcanton J. J., 2000, [ApJ](#), **534**, 146

van der Kruit P. C., Freeman K. C., 1984, [ApJ](#), **278**, 81

This paper has been typeset from a $\mathrm{T}_{\mathrm{E}}\mathrm{X}/\mathrm{L}^{\mathrm{A}}\mathrm{T}_{\mathrm{E}}\mathrm{X}$ file prepared by the author.